



**HAL**  
open science

## High CO<sub>2</sub> content in magmas of the explosive andesitic Enco eruption of Mocho-Choshuenco volcano (Chile)

Jean-Guillaume Feignon, Nicolas Cluzel, Federica Schiavi, Séverine Moune, Olivier Roche, Jorge Clavero, Pierre Schiano, Marion Auxerre

### ► To cite this version:

Jean-Guillaume Feignon, Nicolas Cluzel, Federica Schiavi, Séverine Moune, Olivier Roche, et al.. High CO<sub>2</sub> content in magmas of the explosive andesitic Enco eruption of Mocho-Choshuenco volcano (Chile). *Bulletin of Volcanology*, 2022, 84 (4), pp.40. 10.1007/s00445-022-01550-y . insu-03643025

**HAL Id: insu-03643025**

**<https://insu.hal.science/insu-03643025>**

Submitted on 20 Apr 2022

**HAL** is a multi-disciplinary open access archive for the deposit and dissemination of scientific research documents, whether they are published or not. The documents may come from teaching and research institutions in France or abroad, or from public or private research centers.

L'archive ouverte pluridisciplinaire **HAL**, est destinée au dépôt et à la diffusion de documents scientifiques de niveau recherche, publiés ou non, émanant des établissements d'enseignement et de recherche français ou étrangers, des laboratoires publics ou privés.



Distributed under a Creative Commons Attribution 4.0 International License



# High CO<sub>2</sub> content in magmas of the explosive andesitic Enco eruption of Mocho-Choshuenco volcano (Chile)

Jean-Guillaume Feignon<sup>1,2</sup> · Nicolas Cluzel<sup>1</sup> · Federica Schiavi<sup>1</sup> · Séverine Moune<sup>1,3,4</sup> · Olivier Roche<sup>1</sup> · Jorge Clavero<sup>5</sup> · Pierre Schiano<sup>1</sup> · Marion Auxerre<sup>1,6</sup>

Received: 7 February 2022 / Accepted: 2 March 2022 / Published online: 23 March 2022  
© The Author(s) 2022

## Abstract

Mocho-Choshuenco volcano has produced several highly explosive eruptions during its history, which make it one of the most hazardous volcanoes in the southern volcanic zone of Chile, although it is still relatively little studied to date. We present a geochemical study of the products of the sub-Plinian, andesitic, Enco eruption that occurred about 1600 years ago. We determined the major and trace elements compositions, as well as the volatile (H<sub>2</sub>O, CO<sub>2</sub>, Cl, and S) contents of melt inclusions trapped in minerals (olivine, plagioclase, and pyroxene) using electron microprobe, ion microprobe (SIMS), and 3D confocal Raman mapping. Though the whole-rock composition of the Enco magma is andesitic (60.2 ± 1.1 wt.% SiO<sub>2</sub>), the melt inclusions have SiO<sub>2</sub> contents ranging from 50.3 to 67.3 wt.%, following the magmatic series of Mocho-Choshuenco, and the compositions of the most mafic melt inclusions are close to those of the most mafic erupted magmas. Geochemical modeling indicates that mixing occurred between a mafic magma and an andesitic-to-dacitic magma. Glass analysis revealed typical parental arc magma values for H<sub>2</sub>O (2.6–3.8 wt.%), S (116–1936 ppm), and Cl (620–1439 ppm). However, CO<sub>2</sub> contents are very high in some melt inclusions with concentrations above 4000 ppm (measured in the glass), suggesting trapping depths > ~17–22 km. Presence of solid carbonates inside inclusion-hosted bubbles clearly indicates that the CO<sub>2</sub> contents measured in the glass phase were minimum values. We conclude that a CO<sub>2</sub>-rich basaltic magma ascended and mixed with a shallower andesitic magma. The magma cooled and exsolved high amounts of CO<sub>2</sub>, which may have dramatically increased the pressure and triggered the highly explosive Enco eruption.

**Keywords** Carbon dioxide · Mocho-Choshuenco · Magma volatile content · Explosive eruption · 3D Raman mapping · Melt inclusions

Editorial responsibility: T.P. Fischer; Deputy Executive Editor: J. Tadeucci

✉ Jean-Guillaume Feignon  
jean-guillaume.feignon@univie.ac.at

- <sup>1</sup> Laboratoire Magmas Et Volcans, Université Clermont Auvergne, CNRS, IRD, OPGC, 63000 Clermont-Ferrand, France
- <sup>2</sup> Department of Lithospheric Research, University of Vienna, Althanstrasse 14, 1090 Vienna, Austria
- <sup>3</sup> Institut de Physique du Globe de Paris, CNRS, Université de Paris, 75005 Paris, France
- <sup>4</sup> Institut de Physique du Globe de Paris, Observatoire Volcanologique Et Sismologique de Guadeloupe, 97113 Gourbeyre, France
- <sup>5</sup> Amawta Geoconsultores, Almirante Pastene 185 Of. 503, Providencia, Santiago, Chile
- <sup>6</sup> Centre de Recherches Pétrographiques Et Géochimiques (CRPG), UMR CNRS 5873, Université de Lorraine, BP20, 54501 Vandœuvre les Nancy, France

## Introduction

Various parameters and/or properties may influence the explosivity of a volcanic system (e.g., Sparks et al. 1977; Gonnermann and Manga 2007; Scandone et al. 2007; Deegan et al. 2010; Williamson et al. 2010; Costa et al. 2013; Zimanowski et al. 2015; Cassidy et al. 2018). Differentiated magmas have high viscosities, which, combined with common high volatile contents (if magmas are not degassed), favor the development of high exsolved-gas pressure, and promote efficient magma fragmentation (Williamson et al. 2010; Costa et al. 2013). In contrast, poorly differentiated, low-viscosity magmas with (presumably) lower volatile contents commonly lead to eruptions dominated by effusive rather than explosive dynamics (Huppert and Woods 2002; Gardner 2009). However, examples of highly explosive eruptions involving basaltic to andesitic magmas (SiO<sub>2</sub> < ~60 wt. %) are reported in the literature, e.g., Fuego (Guatemala);

Pozzolane Rosse and Etna (Italy; Coltelli et al. 1998; Métrich et al. 2004; Spilliaert et al. 2006; Freda et al. 2010; Moretti et al. 2018); Masaya (Nicaragua; Szramek 2016); Llaima, Hudson, and Villarica (Chile; Stern et al. 2007); Tarawera (New Zealand; Houghton et al. 2004); the 1790 Keanakakoi eruption at Kilauea (Hawaii; McPhie 1990; Swanson et al. 2012); and Sunset Crater (Arizona; Allison et al. 2021). Possible causes of the high explosivity of these magmas are fast ascent and low degassing rates in the conduit (Zhang 1999), magma-water or ice interaction (Swanson et al. 2012), high magma viscosity due to high crystallinity (Lavallée et al. 2007), and unusually high volatile contents (Sable et al. 2006; Cross et al. 2014). An increasing number of studies have pointed out that highly explosive mafic magmas may also have high CO<sub>2</sub> (and to a lesser extent S and Cl) contents (e.g., Blundy et al. 2010; Aiuppa et al. 2011; Dallai et al. 2011; Freda et al. 2010; Allison et al. 2021). The low solubility of CO<sub>2</sub> (Bottinga and Javoy 1990; Le Gall and Pichavant 2016; Laporte et al. 2016), in particular, may be one of the key factors in promoting explosive dynamics of poorly differentiated magmas.

The relatively poorly studied, and dangerous Mocho-Choshuenco (Chile) represents another case of a volcano presenting explosive eruptions fed by basaltic to andesitic magmas. To better disentangle the origin of its explosive behavior and bring new data on the local magmatism, we focused our investigations on the volatile content of the products of a recent explosive eruption: the Enco-MC15 (as defined by Rawson et al. 2015) eruption. We considered this event because it generated the most mobile pyroclastic flows of the recent eruptive history of Mocho-Choshuenco. In addition, field observations do not provide evidence of phreato-magmatism (Rawson et al. 2015, and our own work), hence excluding a crucial role of magma-water or magma-ice interaction in the explosive character of this eruption. We characterized major, trace, and volatile element compositions of olivine-, pyroxene-, and plagioclase-hosted melt inclusions in order to determine the pre-eruptive conditions of the magmas that fed the Enco-MC15 eruption at Mocho-Choshuenco. Finally, we present a possible scenario of the magmatic storage conditions and the key factors controlling the explosive behavior of the eruption.

## Geological background and sampling

Mocho-Choshuenco volcano (2422 m a.s.l.) is located in Chile (39° 55'S 72° 2'W) in the Southern Volcanic Zone (SVZ) of the Andes (Moreno and Lara 2007; Fig. 1). This volcano has been characterized by 75 post-glacial (< 18 ky) mainly andesitic to dacitic eruptions, including Plinian events that occurred during the Neltume (11 ka–5.3 km<sup>3</sup> fall-out deposit), the Pirehueico (9 ka–2.0 km<sup>3</sup> fallout deposit), the Enco-MC15, and the 1864 AD eruptions (Rawson et al.

2015). The Neltume and Pirehueico eruptions probably led to a partial collapse of the edifice, forming a 4-km-wide caldera that was later filled by successive tephra falls and pyroclastic flow deposits forming the El Mocho cone (Rawson et al. 2015). The total magma volume emitted during the last 18 ky was estimated to ~20 km<sup>3</sup>, making this volcano the most productive of the SVZ (Rawson et al. 2015). It represents a major hazard as more than 400 000 people are living in a 100 km area from the volcano (Rawson et al. 2015). The Enco-MC15 sub-Plinian eruption (Rawson et al. 2015) emitted ~1.7 km<sup>3</sup> of andesitic magma and generated pyroclastic fall and flow deposits. This event generated the most highly mobile pyroclastic flows of the recent eruptive history of Mocho-Choshuenco, with run-out distances of at least ~27 km from the vent in the eastern sector (Clavero et al. 2008).

We sampled an outcrop of a pyroclastic flow deposit of the Enco-MC15 eruption which belongs to unit UM4-5 as defined by Rawson et al. (2015). This outcrop, named VMJ32 in our study, is located on the Eastern flank of Mocho-Choshuenco volcano, 13 km away from the summit vent (Fig. 1). It is composed of several flow units whose tops are outlined by large (10–30 cm) scoria. The material is composed of coarse (mean grain size,  $\phi = -3.35$  to  $-2.54$ ) and well-sorted (sorting,  $\sigma_{\phi} = 1.16$  to  $1.24$ ) juvenile pyroclasts, and rare (< 5 vol. %) lithic clasts. The upper part of these flow units was sampled in the framework of this study. We found charcoal whose <sup>14</sup>C dating gave an age of 1750 ± 40 BP (performed by Beta Analytic Inc., USA). After calibration using OxCal and the southern hemisphere calibration curve SH13 (Ramsey 2009), the age obtained is 1622 ± 86 BP. This is overlapping and consistent with calibrated ages of 1580 ± 115 BP given by Rawson et al. (2015) and Fontijn et al. (2016). Major element compositions of the whole rock samples were analyzed by ICP-AES at Laboratoire Magmas et Volcans, Clermont-Ferrand, France (Table 1, ± 10% relative error at the 2σ level). We focused our study on melt inclusion analysis, and the methods we used are presented below.

## Analytical methods

### Preparation of the melt inclusions

The lapilli-sized (main fraction between 8 and 16 mm with few larger (up to > 32 mm) lapilli) pyroclasts yielding the most suitable phenocrysts to extract for investigation were selected. After crushing and sieving, the > 300 μm fraction was retained to separate phenocrysts from the glass. Olivines and pyroxenes were separated by density using Bromoform (CHBr<sub>3</sub>), whereas the remaining plagioclases and glass were separated magnetically using a FRANTZ magnetic separator.

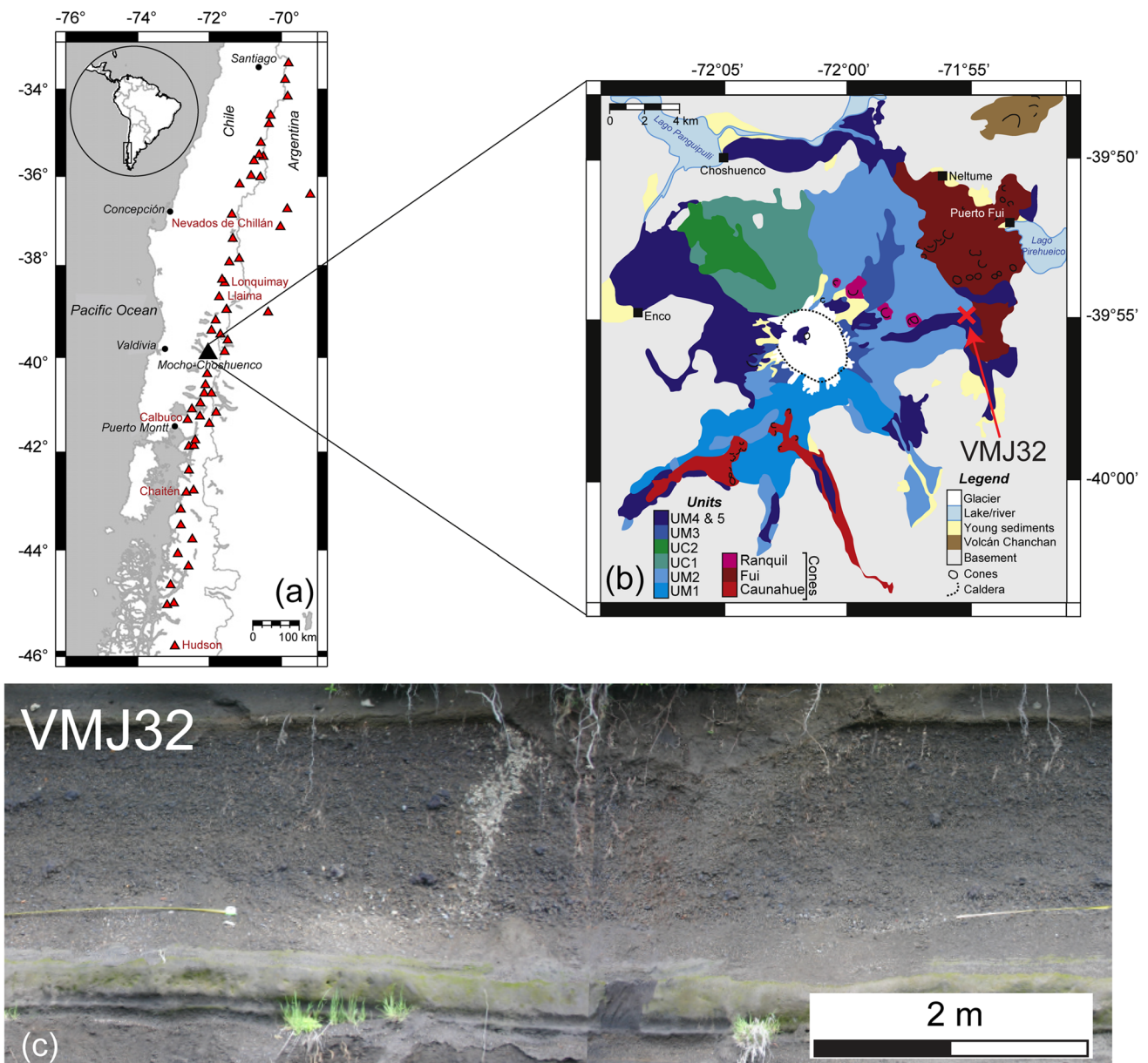


**Fig. 1** **a** Map of the Southern Volcanic Zone (SVZ) with the main Holocene volcanic centers (modified from Rawson et al. 2015). **b** Simplified geological map of Mocho-Choshuenco volcano: units UM1 (> 350–200 ka), UM2 (< 200–130 ka), UC1 (> 100 ka), UC2 (80–20 ka), UM3 (> 60 ka), UM4-5 (18 ka to present). The outcrop of the pyroclastic flow deposit of the unit

Enco-MC15 considered in this study is located in unit UM4-5 and is called VMJ32 (modified from Rawson et al. 2015). **c** Photograph of outcrop VMJ32 showing a coarse-grained pyroclastic flow deposit of the Enco eruption between finely grained surge units. The material analyzed was sampled from juvenile material located in the upper part of the outcrop. The measuring tape is two meters long

The selected crystal-hosted melt inclusions (hereafter denoted as MIs) were glassy, ellipsoidal, with shrinkage bubble(s) and no cracks. Inclusions aligned within fracture planes in the host minerals, due to late melt infiltration, were excluded.

**Electron microprobe**

Following the method of Moune et al. (2012), the major and volatile (S, Cl, and F) element compositions of 41 MIs,

of the host crystals, and of the groundmass glasses were analyzed using a SX-100 CAMECA electron microprobe at Laboratoire Magmas et Volcans, Clermont-Ferrand (France) with a 15 kV accelerating voltage. Analyses of glass samples were done using a probe current of 8 nA for major elements and 40 nA for sulfur, chlorine, and fluorine volatile species, with a defocused beam of 5, 10, or 20 μm according to the size of the MIs. For each sample, prior to sulfur concentration measurement, the S Kα peak maximum was

**Table 1** Whole rock and melt inclusion compositions including host composition. The olivine-hosted melt inclusion compositions were corrected from post entrapment crystallization, while plagioclase- and pyroxene-hosted MIs are uncorrected (i.e., measured value). Uncorrected data for olivine-hosted MIs can be found in Supplementary Material S4. Major oxides and H<sub>2</sub>O given in wt.%, and S, Cl, and CO<sub>2</sub> measured in the MI glass given in ppm. Total Fe is expressed as FeO\*. PEC is expressed as FeO\*. PEC post entrapment crystallization of the host mineral. The K<sub>D</sub> expressed for plagioclase corresponds to the plagioclase (Albite-Anorthite)-liquid equilibrium as expressed by Putirka (2008). *b.d.l.* below detection limit

Sample	Host com- position	SiO <sub>2</sub>	TiO <sub>2</sub>	Al <sub>2</sub> O <sub>3</sub>	FeO*	MnO	MgO	CaO	Na <sub>2</sub> O	K <sub>2</sub> O	P <sub>2</sub> O <sub>5</sub>	Total	S	Cl	H <sub>2</sub> O	CO <sub>2</sub>	K <sub>b</sub>	PEC (%)	
<b>Whole rock</b>																			
VMJ32		60.2	1.19	16.3	7.57	0.17	2.22	5.35	4.79	1.29	0.40	99.74	-	-	-	-	-	-	-
<b>Groundmass (n = 8)</b>																			
VMJ32		61.5	1.26	15.6	6.78	0.25	2.09	5.06	4.68	1.56	0.38	99.08	138	986	-	-	-	-	-
<b>Olivine-hosted inclusions</b>																			
<b>Fo</b>																			
O11_MI1	80	51.0	1.15	19.9	6.62	0.25	3.61	10.0	3.27	0.59	0.11	96.54	1535	628	2.83	214	0.17	4.5	4.5
O12_MI1	78	53.6	1.35	18.6	6.15	b.d.1	3.08	9.27	4.09	0.81	0.25	97.17	1610	675	2.99	541	0.16	4.0	4.0
O16-4_MI1	81	51.5	0.99	18.9	6.84	0.15	4.41	9.62	3.22	0.58	0.08	96.21	1529	637	2.87	873	0.19	5.0	5.0
O16-5_MI1	78	51.2	1.11	18.6	7.03	0.02	4.23	9.32	3.32	0.60	0.35	95.81	1516	684	2.62	2836	0.23	3.0	3.0
O16-9_MI1	76	52.2	1.05	18.2	5.73	0.02	5.15	9.03	3.71	0.67	0.38	96.18	605	-	-	-	0.10	9.0	9.0
O16-12_MI1	77	55.9	1.82	15.2	6.59	0.08	3.21	7.10	4.81	1.28	0.28	96.28	1341	1118	-	-	0.14	5.0	5.0
O16-13_MI1	75	53.2	1.17	18.1	7.39	0.10	3.18	8.94	3.53	0.70	0.23	96.49	1936	692	0.48	225	0.23	2.5	2.5
O16-14_MI1	81	50.6	1.11	19.1	6.80	0.15	4.28	9.69	3.22	0.60	0.28	95.87	1594	625	2.73	636	0.18	5.0	5.0
O16-14_MI2	81	51.9	1.05	18.6	6.77	b.d.1	4.39	9.41	3.33	0.60	0.22	96.29	1494	638	-	-	0.17	5.5	5.5
O16-15_MI1	81	52.2	1.07	18.7	6.84	0.13	4.05	9.38	3.39	0.62	0.20	96.48	1485	662	3.10	283	0.24	2.5	2.5
M16	76	50.3	1.00	18.0	8.13	0.12	5.05	9.71	3.01	0.51	0.21	96.01	1220	620	-	-	0.14	8.0	8.0
<b>Plagioclase-hosted inclusions</b>																			
<b>An</b>																			
P11_MI1	50	62.3	0.83	14.0	4.66	0.43	1.37	3.62	3.64	1.77	0.35	92.95	200	1223	2.85	4213	0.14	0.14	0.14
P12_MI1	76	56.3	1.49	14.3	8.09	0.26	3.39	5.33	4.03	1.46	0.33	94.99	1184	1045	3.84	1075	0.07	0.07	0.07
P13_MI1	50	64.8	0.80	15.7	4.85	0.16	1.01	3.35	4.81	1.83	0.26	97.54	181	1223	2.78	212	0.11	0.11	0.11
P14_MI1	51	65.9	0.78	15.4	4.39	0.03	1.15	3.27	5.04	1.80	0.31	98.00	120	1142	1.21	473	0.09	0.09	0.09
P15_MI1	50	65.5	0.63	15.6	3.90	0.16	0.92	2.95	5.33	1.91	0.24	97.10	129	1019	-	-	0.08	0.08	0.08
P16_MI1	48	64.4	0.71	15.9	4.12	0.18	0.99	3.26	4.93	1.79	0.22	96.51	114	1075	2.84	2710	0.11	0.11	0.11
P17_MI1	50	60.8	0.97	15.5	5.93	0.17	2.11	4.36	4.95	1.64	0.37	96.79	273	969	3.16	321	0.14	0.14	0.14
P17_MI2	50	64.4	0.77	15.9	4.62	0.11	1.21	3.33	4.67	1.82	0.07	96.96	212	1240	2.66	860	0.11	0.11	0.11
P1M1_MI1	49	64.1	0.72	15.8	4.57	0.07	1.07	3.15	5.26	1.86	0.28	96.90	170	1124	2.48	4430	0.10	0.10	0.10
P1M4_MI1	47	62.8	0.98	16.0	5.67	0.16	1.26	3.49	3.93	1.85	0.31	96.43	243	1309	1.85	689	0.16	0.16	0.16
M2	49	63.1	0.82	15.5	4.94	0.16	1.11	3.11	5.03	2.05	0.46	96.29	172	1373	-	-	0.10	0.10	0.10
M4	49	60.7	1.27	14.8	6.84	0.16	1.99	4.28	4.79	1.74	0.61	97.17	434	1174	-	-	0.11	0.11	0.11
M6	48	65.8	0.62	15.2	3.30	0.10	0.95	2.96	4.93	1.60	0.12	95.61	115	773	-	-	0.07	0.07	0.07
M8	44	66.0	0.69	15.2	4.42	0.18	0.97	2.95	5.10	1.72	0.12	97.33	117	1099	-	-	0.10	0.10	0.10
M15	45	64.4	0.58	14.7	4.74	0.09	1.13	3.08	5.06	1.73	0.35	95.85	160	1262	-	-	0.09	0.09	0.09

**Table 1** (continued)

Sample	Host com- position	SiO <sub>2</sub>	TiO <sub>2</sub>	Al <sub>2</sub> O <sub>3</sub>	FeO*	MnO	MgO	CaO	Na <sub>2</sub> O	K <sub>2</sub> O	P <sub>2</sub> O <sub>5</sub>	Total	S	Cl	H <sub>2</sub> O	CO <sub>2</sub>	K <sub>D</sub>	PEC (%)	
M20a	50	62.5	0.95	15.5	5.01	0.20	1.19	3.21	4.94	1.78	0.38	95.66	241	1364	-	-	0.12		
M24	49	64.1	0.72	15.5	4.30	0.19	1.18	3.45	5.02	1.87	0.09	96.41	169	1310	-	-	0.12		
M1	51	62.9	0.52	15.2	4.46	0.20	1.18	3.29	4.77	1.93	0.20	94.65	154	1221	-	-	0.09		
M3	49	62.6	0.74	15.2	4.12	0.07	1.12	3.11	5.25	2.08	0.35	94.72	189	1393	-	-	0.09		
M11	50	66.2	0.62	15.0	4.00	0.17	0.91	2.96	5.25	1.79	0.18	97.08	147	999	-	-	0.08		
M12	50	63.7	0.79	15.1	4.41	0.16	1.05	3.11	5.08	1.95	0.26	95.60	174	1188	-	-	0.09		
M14	48	63.8	0.40	15.5	4.08	0.21	1.01	3.08	5.45	1.65	0.12	95.25	141	1123	-	-	0.09		
M25	49	59.3	1.22	14.8	6.52	0.24	2.34	4.55	4.43	1.47	0.26	95.10	242	1025	-	-	0.17		
<b>Pyroxene-hosted inclusions</b>																			
<b>En</b>																			
M10	67	67.3	0.75	14.2	4.14	0.15	0.78	2.56	4.21	1.91	0.18	96.09	116	1182	-	-	0.14		
M20b	59	64.3	1.22	14.0	4.75	0.21	0.51	2.53	3.69	1.87	0.35	93.44	156	1439	-	-	0.12		
M7a	42	58.6	1.30	15.7	7.61	0.24	1.99	5.20	4.77	1.32	0.78	97.54	712	1058	-	-	0.20		
M7b	42	61.5	1.51	15.7	5.34	0.14	1.02	3.21	5.43	1.90	0.53	96.22	177	1308	-	-	0.24		
M7c	42	61.3	0.94	15.8	5.64	0.10	1.28	3.37	4.99	1.55	0.58	95.54	278	1230	-	-	0.25		
M7d	42	63.1	1.16	16.0	5.38	0.23	1.55	3.89	4.53	1.43	0.41	97.66	303	1333	-	-	0.22		
M7e	42	61.5	1.33	15.3	6.24	0.30	1.59	3.82	4.48	1.47	0.23	96.26	327	1151	-	-	0.20		

first located by using the automated peak-scan routine, and the value of the peak position was recorded in the analysis setup (as described in Rose-Koga et al. 2020). Variations in the wavelength of sulfur K $\alpha$  X-ray as a function of its oxidation state in silicate glasses (Wallace and Carmichael 1994; Métrich and Clocchiatti 1996) were taken into account during S analysis. For minerals analyses, the beam current was 15 nA, and the beam size was 1  $\mu\text{m}$ . Spots were both acquired at the edge of the inclusions and at the mineral rim. The precision of the electron microprobe ( $2\sigma$ ) was less than 10% for major elements, except for MnO, TiO<sub>2</sub>, and P<sub>2</sub>O<sub>5</sub>, and it was 6% for S and Cl. Fluorine data were excluded as they were all below the detection limit (< 370 ppm).

### Mass spectrometry (SIMS and LA-ICPMS)

MIIs larger than 40  $\mu\text{m}$  in diameter were selected for mass spectrometry analysis. H<sub>2</sub>O and CO<sub>2</sub> contents of 16 MIIs (7 olivine- and 9 plagioclase-hosted) were analyzed using the CAMECA IMS 1270 Ion Probe (SIMS) at the Centre de Recherches Pétrographiques et Géochimiques, Nancy (France), with a 15- $\mu\text{m}$  beam size for all analyses. Pyroxene-hosted MIIs were not selected for SIMS and LA-ICPMS analysis being their size lower than the beam size. The selected crystals were transferred directly to indium sample holders, and no electron microprobe analyses were performed before using the SIMS in order to avoid carbon-coating contamination. Samples were gold coated and held in a gas chamber for degassing and cleaning (“pre-sputtering”). The glasses were sputtered with a 10 kV Cs<sup>+</sup> primary beam of 10–15 nA. When a high CO<sub>2</sub> (> 1500 ppm) content was detected, the analysis was performed three times to check for any possible carbon contamination. Before and after each analytical session, a series of international reference standard basaltic and andesitic glasses were used for calibration of water and carbon contents (measurements on standard material and calibration curves are available in Supplementary Material S1). The error ( $2\sigma$ ) was 1.5% for H<sub>2</sub>O and 15% for CO<sub>2</sub>.

In situ trace element analyses of 10 MIIs (4 olivine- and 6 plagioclase-hosted) were performed by laser ablation inductively coupled-plasma mass-spectrometry (LA-ICPMS) at Laboratoire Magmas et Volcans using a Resonetics M50 Excimer Laser with a 193-nm wavelength coupled to an ICPMS Agilent 7500cs. Raw data were processed with Glitter Software using CaO content as an internal standard (see method details and analytical errors in Venugopal et al. 2016).

### Raman spectrometry

Raman measurements were carried out at the Laboratoire Magmas et Volcans using a Renishaw inVia confocal microspectrometer equipped with a 532-nm diode laser, a

Peltier-cooled CCD detector, and a Leica DM 2500 M optical microscope with a motorized XYZ stage. Scattered light was collected in a back-scattered geometry. Laser power on the sample was reduced to 8–16 mW to avoid damaging the samples. A 2400 lines/mm grating, a 20- $\mu\text{m}$  slit aperture (high confocality setting), and a 100 $\times$  microscope objective were used for the analyses. These analytical conditions resulted in spectral resolution of  $\sim 0.5\text{ cm}^{-1}$  and lateral spatial resolution of  $\sim 1\text{ }\mu\text{m}$ . Vertical resolution was  $\sim 2\text{--}3\text{ }\mu\text{m}$  near the surface but deteriorated with depth mainly due to light refraction at the air/glass/bubble interfaces. Daily calibration of the spectrometer was performed based on the 520.5  $\text{cm}^{-1}$  peak of Si.

Two- or three-dimensional Raman mapping was performed on four MI-hosted bubbles. The 2D maps were acquired in the plane of the maximum bubble diameter with a step size of 1  $\mu\text{m}$ . For 3D maps, we first performed depth profiles to define the vertical dimension of the map. The step size between acquisition points was 1 or 2  $\mu\text{m}$  on the x- and y-axis and 2  $\mu\text{m}$  on the z-axis. The acquisition time ranged from 20 to 60 s/point, and the spectra were continuously collected over 3 days in the  $\sim 200\text{--}1400\text{ cm}^{-1}$  wavenumber range. Each 3D mapping produced a single hypermap of several thousand of spectra that was processed using WiRE™ 4.2 software. We applied a polynomial baseline correction to the entire dataset. For each phase present in the bubble, we selected a characteristic peak, whose intensity variations in the analyzed volume informed about the spatial distribution of that phase in the bubble. The intense peak located between 1085 and 1097  $\text{cm}^{-1}$  (Frezzotti et al. 2012) was used to map solid carbonates (Mg-calcite, magnesite, dolomite, and siderite), while a few grains of sulfides showing peaks near 320, 340, and 370  $\text{cm}^{-1}$  were identified as either pyrrhotite or pyrite. The Fermi doublet peaks of fluid CO<sub>2</sub> at  $\sim 1286$  and 1388  $\text{cm}^{-1}$  were barely recognizable in some spectra as their intensities remained very weak, most likely due to low fluid density. The calibration by Lamadrid et al. (2017) was used to determine CO<sub>2</sub> density.

Several 2D sections along the z-axis were processed using Image J software to obtain the area fractions of each phase present inside the bubble. To estimate the volumetric fraction of each phase, the area fraction in each section was multiplied by the vol% of the associated spherical segment (i.e., the volume between adjacent x–y sections), and then the volumetric fractions of each phase in all spherical segments were summed (for further details, the reader is referred to Schiavi et al. 2020). The mass of carbonates was estimated from the measured volume and assuming a mean carbonate density value of 3.2  $\text{g/cm}^3$ . The total CO<sub>2</sub> concentration in a MI was given by the sum of the CO<sub>2</sub> dissolved in the melt and the CO<sub>2</sub> contained in the bubble. The inclusion volume was calculated assuming that inclusion thickness is equal to the arithmetic mean of the two

inclusion axes visible in the polished plane, as it seems to be the most accurate method (Tucker et al. 2019). The errors associated with the estimated inclusion volume and CO<sub>2</sub> concentration are relatively high because they include the uncertainties related to the spatial resolution of the technique, the decreasing intensity of the Raman signal with depth, the approximation of the applied geometric model, and the assumption about phase densities (more details on the method can be found in Supplementary Material S2 and in Schiavi et al. 2020).

## Results

### Petrography and textures of the melt inclusions

Samples contain plagioclase (mainly), clinopyroxene, olivine, rare orthopyroxene phenocrysts, and bubbles (see Supplementary Material S3). The phenocrysts represent ~5–10 vol.% of the whole rock. Finely crystallized plagioclase xenoliths are rare. Amphibole is absent, suggesting no excess of water. The microlites represent ~15–25 vol.% of the groundmass, whereas the vesicularity is ~30–40 vol.%. Figure 2 shows some of the textures commonly observed in MIs analyzed in this study. Three MI textures are identified in all studied host phases: (1) the typical rounded glassy case with one shrinkage bubble occupying less than 10% of the MI volume (Fig. 2a), (2) a shrinkage bubble occupying more than 50% of the inclusion volume (Fig. 2b), and (3) tens to hundreds of small bubbles ~1 to 10 μm in diameter, distributed along the rim or inside the whole MI volume, and occupying 10–50 vol. % of the MI, which are generally associated with a larger shrinkage bubble (Fig. 2c). The two last aforementioned textures represent 55% of the analyzed MIs.

## Compositions of melt inclusions

### Post-entrapment modifications

Following entrapment, MIs can undergo modifications that include bubble formation, host crystallization, chemical diffusion (e.g., Fe and Mg diffusion in olivine- and pyroxene-hosted MIs), formation of daughter minerals, and volatile leakage (Wallace et al. 2015; Le Voyer et al. 2017). All analyzed MIs lacked daughter minerals and were not fractured. Crystallization of the host mineral, however, commonly leads to the formation of an overgrowth rim which may also modify the MI composition (see also, Schiano 2003). The presence of an overgrowth at the MI rim is assumed based on the disequilibrium between the melt and host-crystal given by  $K_D$  values. This rim must be accounted for in order to determine the original melt composition. We used the well-established Fe–Mg distribution coefficient between olivine and melt to correct MIs compositions ( $K_{Dol-melt} = [X_{ol}^{Fe}/X_{ol}^{Mg}] / [X_{melt}^{Fe}/X_{melt}^{Mg}] = 0.30 \pm 0.03$ ; Roeder and Emslie 1970, Toplis 2005). The Fe<sup>3+</sup>/Fe<sub>tot</sub> ratio was calculated to be ~0.2 based on the  $fO_2$  (from NNO-0.5 to NNO + 0.5, Rawson et al. 2015). For the Enco-MC15 Mocho-Choshuenco eruption, the uncorrected  $K_{Dol-melt}$  values obtained from measurements range between 0.10 and 0.24, indicative of post-entrapment crystallization (PEC). The oxide contents of the MIs were corrected by adding olivine (i.e., with the starting composition being the measured composition of olivine to which the MI belongs) incrementally to the inclusion composition until the equilibrium was reached, assuming that these corrected values represent the equilibrium compositions (PEC ranging from 2.5 to 9%). Uncorrected and corrected data for major, trace, and volatile elements composition,  $K_D$  and PEC values are reported

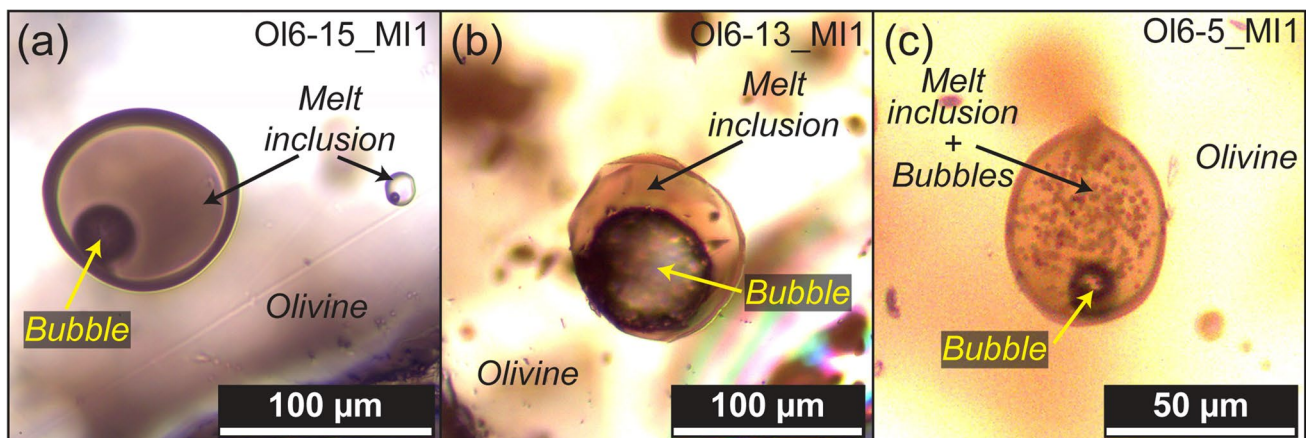


**Fig. 2** Textures of the MIs. The identification of inclusions refers to Table 1. **a** Inclusion Ol6-15\_MI1 with one retraction bubble of small volume. **b** Inclusion Ol6-13\_MI1 with a big bubble (~40% of the

inclusion volume). **c** Inclusions Ol6-5\_MI1 with a shrinkage bubble and numerous small bubbles inside the inclusion



in Table 1 and in Supplementary material S4. Taking into account the PEC, the corrected MI compositions hosted in olivines represent the melt trapped at the time of host crystallization.

Correction of pyroxene- and plagioclase-hosted inclusions from host crystallization is more challenging due to the uncertainty associated with their respective distribution coefficients. The Fe–Mg distribution coefficient between clinopyroxene and MIs measured in the studied samples is  $K_D = 0.20–0.25$ , which is slightly lower, but within the uncertainty of the equilibrium  $K_D$  of  $0.27 \pm 0.08$  provided in literature (Putirka 2008). This suggests that host crystallization of pyroxene within the MIs was minimal. The measured  $K_D$  between orthopyroxene and MIs is equal to  $0.12–0.14$ . Unlike the clinopyroxene-hosted MIs, the calculated  $K_D$  using Putirka (2008) equation ( $K_D^{\text{Fe-Mg}}(\text{opx-liq}) = 0.4805 - 0.3733X_{\text{Si}}^{\text{liq}}$ , where  $X_{\text{Si}}$  is the fraction of silica cation in the melt) is  $\sim 0.30$ , indicating that the orthopyroxene-hosted MIs are not at equilibrium. Consequently, these data were not used for modeling. The  $K_D$  for the plagioclase (albite-anorthite)-liquid equilibrium found in literature is  $0.10 \pm 0.05$  for a magmatic liquid with a temperature less than  $1050^\circ\text{C}$  (Putirka 2008). In our samples, the temperature of the plagioclase-hosted MIs (andesitic composition) is estimated at  $1035 \pm 60^\circ\text{C}$  (see the “[Petrography and textures of the melt inclusions](#)” section), and the observed  $K_D$  is between  $0.07$  and  $0.17$ , suggesting that the melt may be at equilibrium with the host mineral. Taken as a whole, the major element compositions of most of the pyroxene- and plagioclase-hosted MIs follow the trend defined by the bulk-rock samples (Fig. 3), suggesting negligible modification of the original melt composition by post-entrapment crystallization. As no correction was applied to the MIs hosted in pyroxene and plagioclase, the concentrations of volatile and incompatible elements in these inclusions could be slightly higher than the original concentrations in the trapped melt. In this regard, we point out that even a large amount of PEC (i.e., 10%) has a very low impact on concentration of incompatible elements.

### Major and trace element compositions

The whole rock composition is andesitic, with  $60.2$  wt.%  $\text{SiO}_2$ ,  $2.22$  wt.%  $\text{MgO}$ , and  $6.08$  wt.% total alkalis (Table 1). The groundmass glass that represents the last stage in the melt evolution is andesitic and homogeneous, with  $61.5$  wt.%  $\text{SiO}_2$  and  $6.24$  wt.% total alkalis representing the average of eight measurements. The MIs, however, have compositions ranging from basaltic to dacitic depending on the nature of the host mineral. The host olivines have a narrow forsterite range,  $\text{Fo}_{75-81}$  (Table 1). Melt inclusions from the same olivine host do not vary considerably in major element contents. The olivine-hosted MIs have well constrained oxide

contents and are basaltic to basaltic-andesites in composition with:  $50.3–55.9$  wt.%  $\text{SiO}_2$ ,  $3.08–5.15$  wt.%  $\text{MgO}$ , and  $0.51–1.28$  wt.%  $\text{K}_2\text{O}$  (Table 1, Fig. 3). These compositions are more primitive than the whole rock and groundmass glasses. The pyroxene ( $\text{En}_{42-67}$ ) and plagioclase ( $\text{An}_{44-51}$  and one  $\text{An}_{76}$ ) hosted MIs are more evolved, being andesitic to dacitic in composition, with  $56.3–67.3$  wt.%  $\text{SiO}_2$ ,  $0.78–3.39$  wt.%  $\text{MgO}$ , and  $1.43–2.08$  wt.%  $\text{K}_2\text{O}$ . Moreover, these compositions are generally more evolved than those of the groundmass and whole rock. These data can be compared with the eruptive glass compositions at Mocho-Choshuenco that range from ca.  $55$  wt.% to ca.  $73$  wt.%  $\text{SiO}_2$  (Rawson et al. 2015) and the erupted whole rock compositions that range from ca.  $50$  wt.% to ca.  $68$  wt.%  $\text{SiO}_2$  (Rawson et al. 2016). The most mafic MIs compositions, in particular, are close to that of the most mafic erupted magmas, whereas the most evolved MIs are following the general trend of Mocho-Choshuenco erupted magmas.

Trace element compositions in the inclusions show typical arc-like patterns with low concentrations of HFSEs such as Nb, and enrichment in U, Pb, and Ba, as shown in the spider diagram (Supplementary Material S4). The compositional variability of the observed trends is related to the composition of the host minerals, so that the plagioclase-hosted MIs are more enriched in trace elements, whereas more primitive MIs in olivines display lower trace element concentrations.

### Volatile element compositions

The different volatile species show contrasting patterns as a function of the degree of differentiation (i.e., increasing  $\text{K}_2\text{O}$  content, Fig. 4). The  $\text{H}_2\text{O}$  contents in olivine-hosted inclusions range from  $2.62$  to  $3.10$  wt.%, except for an inclusion with a large bubble (O16-13\_MI1,  $0.48$  wt.%). The plagioclase-hosted MIs present a large variability in  $\text{H}_2\text{O}$  content, ranging from  $1.21$  up to  $3.84$  wt.%. The highest  $\text{H}_2\text{O}$  concentration is found in a MI with hundreds of small bubbles hosted in  $\text{An}_{76}$  plagioclase (PI2\_MI1). The plagioclase-hosted MIs show a general trend of decreasing  $\text{H}_2\text{O}$  content with increasing  $\text{K}_2\text{O}$  (Fig. 4c), which is consistent with crystallization accompanied by degassing of a  $\text{H}_2\text{O}$ -saturated magma.

The  $\text{CO}_2$  content measured in the MI glass is below  $1100$  ppm in most cases, independent of the host mineral, but four inclusions show much higher values of  $2836$  ppm in an olivine-hosted MI (O16-5\_MI1), and  $2710$  ppm (PI6\_MI1),  $4213$  ppm (PI1\_MI1), and  $4430$  ppm (PIM1\_MI1) in plagioclase-hosted MIs. Two of the inclusions mentioned above (O16-5\_MI1 and PIM1\_MI1) have several bubbles inside the inclusion (hundreds of them in O16-5\_MI1, see Fig. 2c). The two other inclusions with high  $\text{CO}_2$  content have a regular shape with a shrinkage

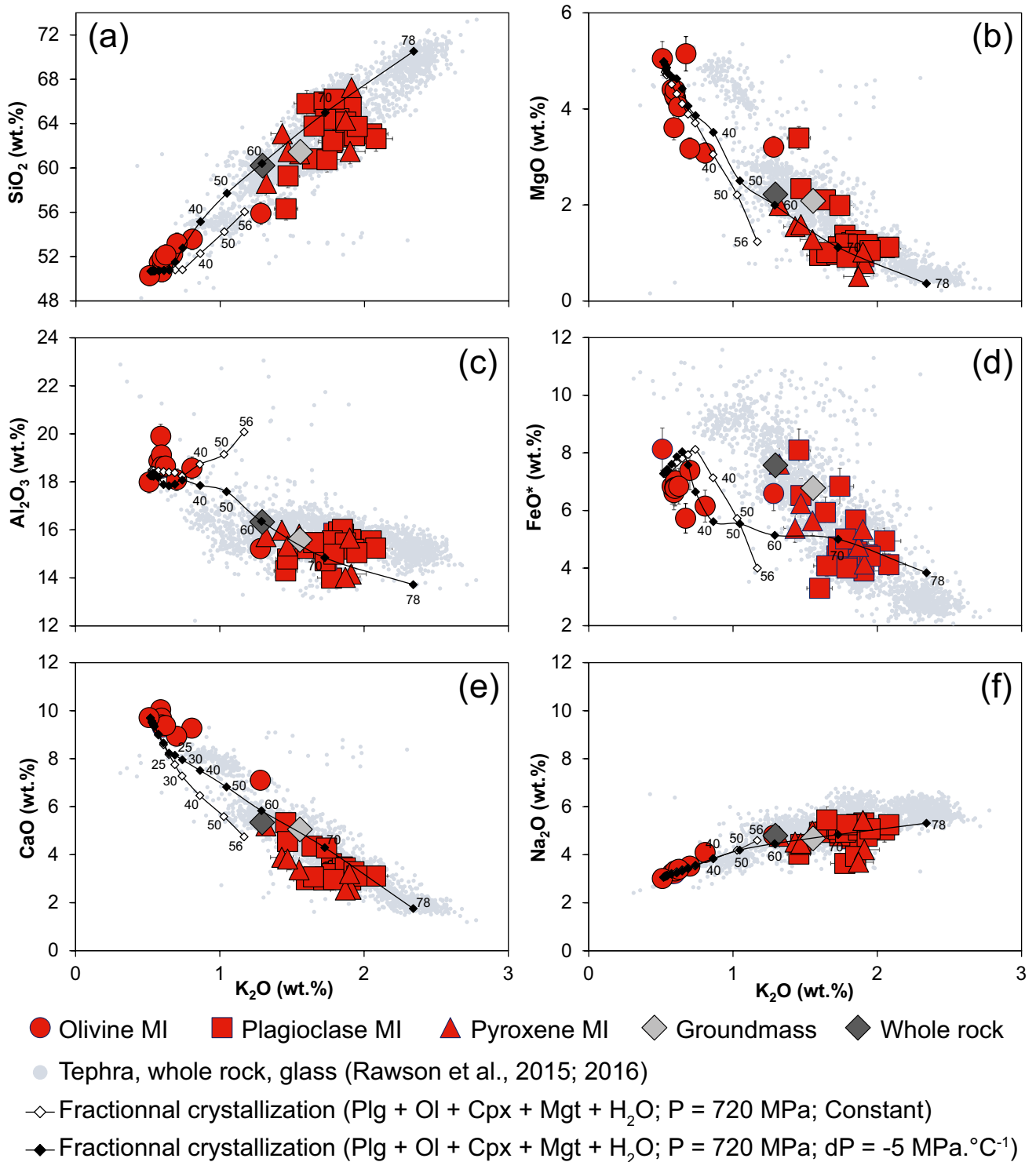


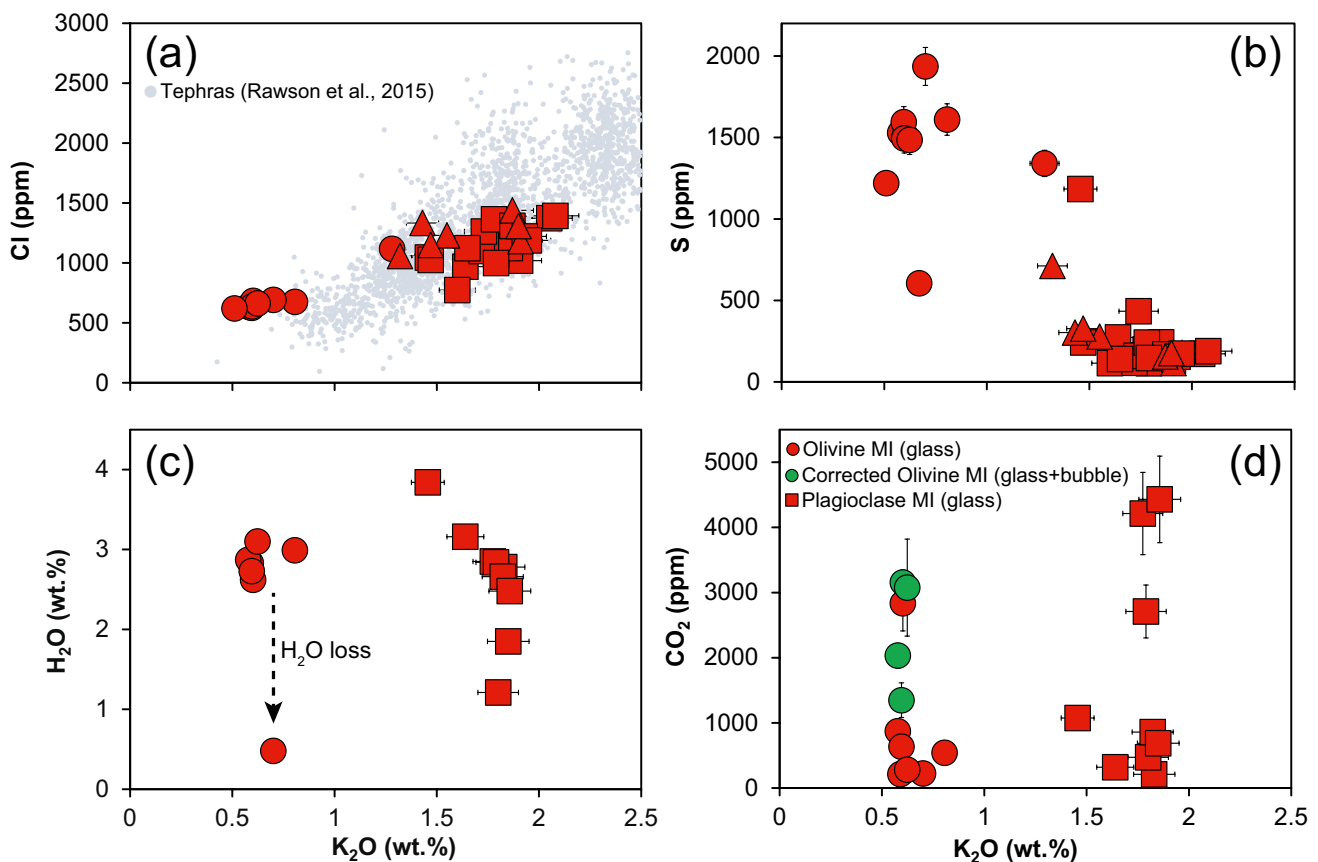
**Fig. 3** a–f Major oxide diagrams of investigated MIs. Olivine-hosted inclusions represent the primitive end-member and the plagioclase-hosted inclusions the most evolved one. The olivine-hosted MIs compositions are corrected from post-entrapment crystallization of host mineral at the rim of the MI. The two curves represent Petrolog3

output of fractional crystallization models. The numbers represent the percentage of fractional crystallization. Diamonds on the fractional crystallization (FC) model curves represent increments with steps of: 1% from 1 to 5% FC, 5% from 5 to 30% FC, and 10% from 30% to the end of the FC. Error bars are  $2\sigma$ . See Table 1 for values

bubble similar to the MI shown in Fig. 2a. Furthermore, it is worth noting that the two other MIs containing more than a hundred of small bubbles (OI6-4\_MI1 and PI2-MI1) have relatively high CO<sub>2</sub> contents in the glass: 873 ppm and 1075 ppm, respectively. Raman analysis of olivine-hosted inclusions containing a shrinkage bubble revealed precipitation of solid carbonates at the rim of the bubble. In the analyzed bubbles (OI6-4\_MI1, OI6-5\_MI1, OI6-14\_MI1, and OI6-15\_MI1 MIs), the volume of the solid carbonates ranges from  $5 \pm 2$  to  $26 \pm 7\%$  of the bubble volume (supplementary material S2). Consequently, the quantity of CO<sub>2</sub> within the bubble represents 41 to 93% of the total amount, excepted for OI6-5 with only 10 to 20% of the CO<sub>2</sub> inside the bubble (see supplementary material S2). Carbonates were observed only in the bubbles of olivine-hosted MIs (Fig. 5). When CO<sub>2</sub> stored in carbonates is taken into account, the corrected values of CO<sub>2</sub> for OI6-4\_MI1, OI6-5\_MI1, OI6-14\_MI1, and OI6-15\_MI1 (Fig. 5) are  $2033 \pm 187$ ,  $3155 \pm 190$ ,  $1348 \pm 266$ , and  $3077 \pm 744$  ppm, respectively (873, 2836, 636, and 283 ppm in the MI glasses, respectively). The presence of carbonates indicates that the CO<sub>2</sub> contents in MIs (glass)

given in Table 1 are minima, underestimated values for olivine-hosted MIs. Our results are in agreement with previous estimates of CO<sub>2</sub> lost in the shrinkage bubble during post-entrapment (15–98%; Anderson and Brown 1993; Moore et al. 2015; Wallace et al. 2015; Robidou et al. 2016; Tucker et al. 2019; Venugopal et al. 2020; Schiavi et al. 2020; Allison et al. 2021). These results suggest that the magma was originally very rich in CO<sub>2</sub>, with contents possibly larger than 4000 ppm.

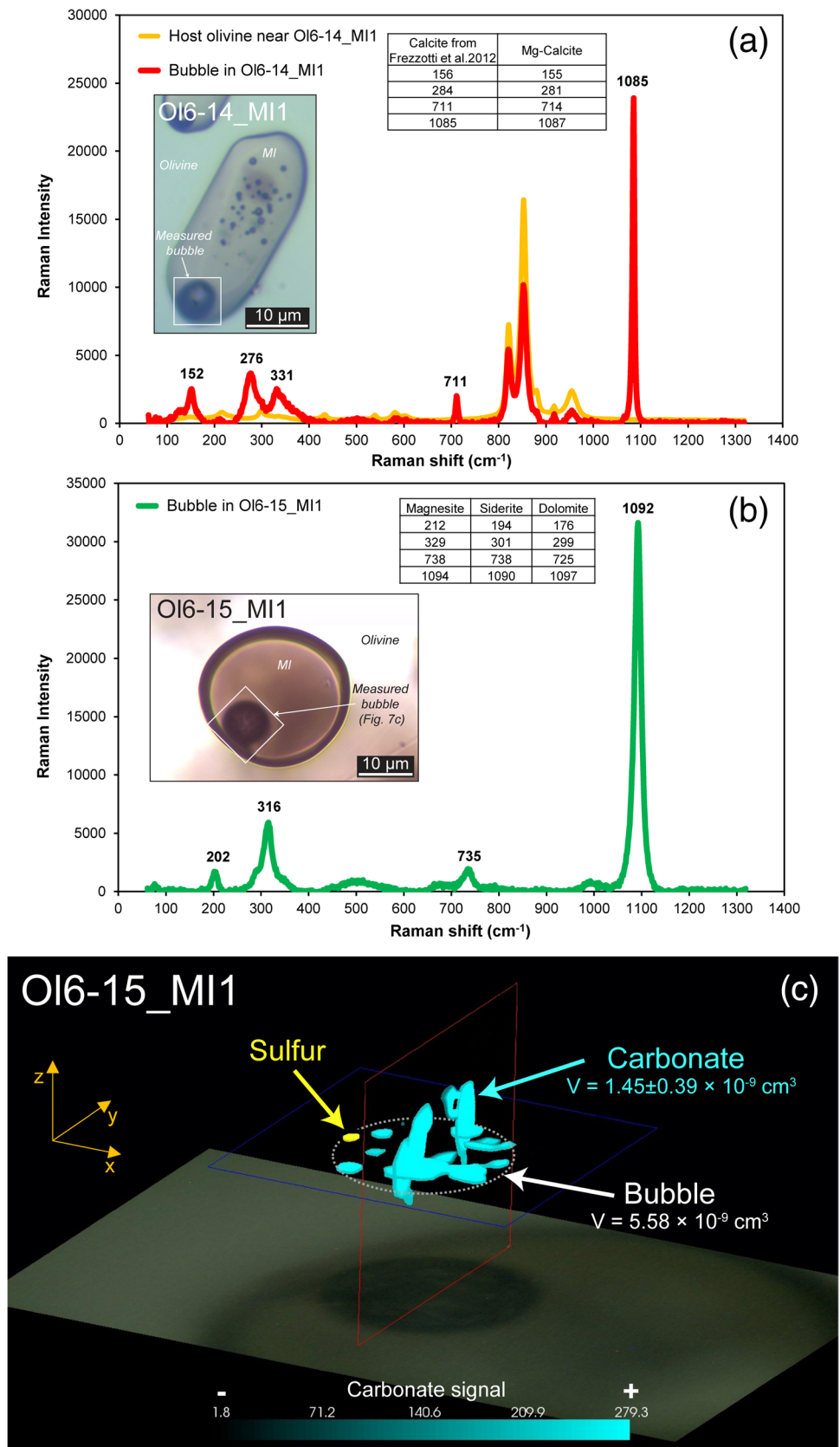
The S content decreases with increasing degree of differentiation (i.e., increasing K<sub>2</sub>O; Fig. 4b). It ranges from 605 to 1936 ppm in olivine-hosted MIs. It is in general lower in pyroxene- and plagioclase-hosted MIs (excepted two inclusions with 712 and 1184 ppm). Considering oxidation conditions at Mocho-Choshuenco between NNO-0.5 and NNO + 0.5 (Rawson et al. 2015), the S content at saturation in basaltic melts is estimated at  $1500 \pm 500$  ppm at 200 MPa (Wallace and Carmichael 1992; Lesne et al. 2015) and is expected to vary from 1500 to 4500 ppm as *f*O<sub>2</sub> increases at ~ 1 GPa (Jugo 2009). The large variability in the S content of the olivine-hosted MIs (Fig. 4b) suggests saturation of the basaltic magma. In contrast, the Cl content generally



**Fig. 4 a–d** Volatile contents relative to K<sub>2</sub>O contents of the studied MIs. For four olivine-hosted MIs, both corrected (bubble + glass) and uncorrected (only glass) CO<sub>2</sub> contents are reported. The variability of S, H<sub>2</sub>O, and CO<sub>2</sub> observed for a given K<sub>2</sub>O value is an evidence of

degassing. The high CO<sub>2</sub> contents in both basaltic and andesitic melts suggest that the two magmas that mixed and fed the Enco eruption were rich in CO<sub>2</sub>

**Fig. 5** **a** Raman spectrum showing the occurrence of solid carbonates in the bubble of OI6-14\_MI1 MI (red spectrum). The olivine-host mineral is represented by the orange spectrum. The numbers in bold and the table indicate the characteristic peaks of calcite and Mg-calcite. A clear, intense peak is centered at  $1085\text{ cm}^{-1}$ . A 3D-mapping was performed in the area with small bubbles, but  $\text{CO}_2$  peaks could not be detected mainly due to the small size of the bubbles ( $< 1\text{--}2\text{ }\mu\text{m}$  in diameter) and probably low  $\text{CO}_2$  density. **b** Typical Raman spectrum from the large bubble of OI6-15\_MI1 MI. As for OI6-14\_MI1, the curve is mainly characterized by an intense and large peak centered at  $1092\text{ cm}^{-1}$ , which indicates the occurrence of different solid carbonates (probably magnesite, siderite, and/or dolomite). The other characteristic peaks for these solid carbonates are indicated in the table. **c** Raman 3D-map of the bubble in the OI6-15 MI, showing the distribution of carbonates inside the bubble. The blue scale represents the number of counts: a high number of counts indicate a high content in solid carbonates (bright blue), whereas dark areas correspond to low carbonates content. In addition, solid carbonates and bubble volumes ( $V$ ) are indicated. The yellow area corresponds to sulfur; S in the bubble is not discussed here; however, it confirms that the bubble is also a reservoir for S, as suggested in Venugopal et al. (2020). A photograph of the bubble is shown below the map



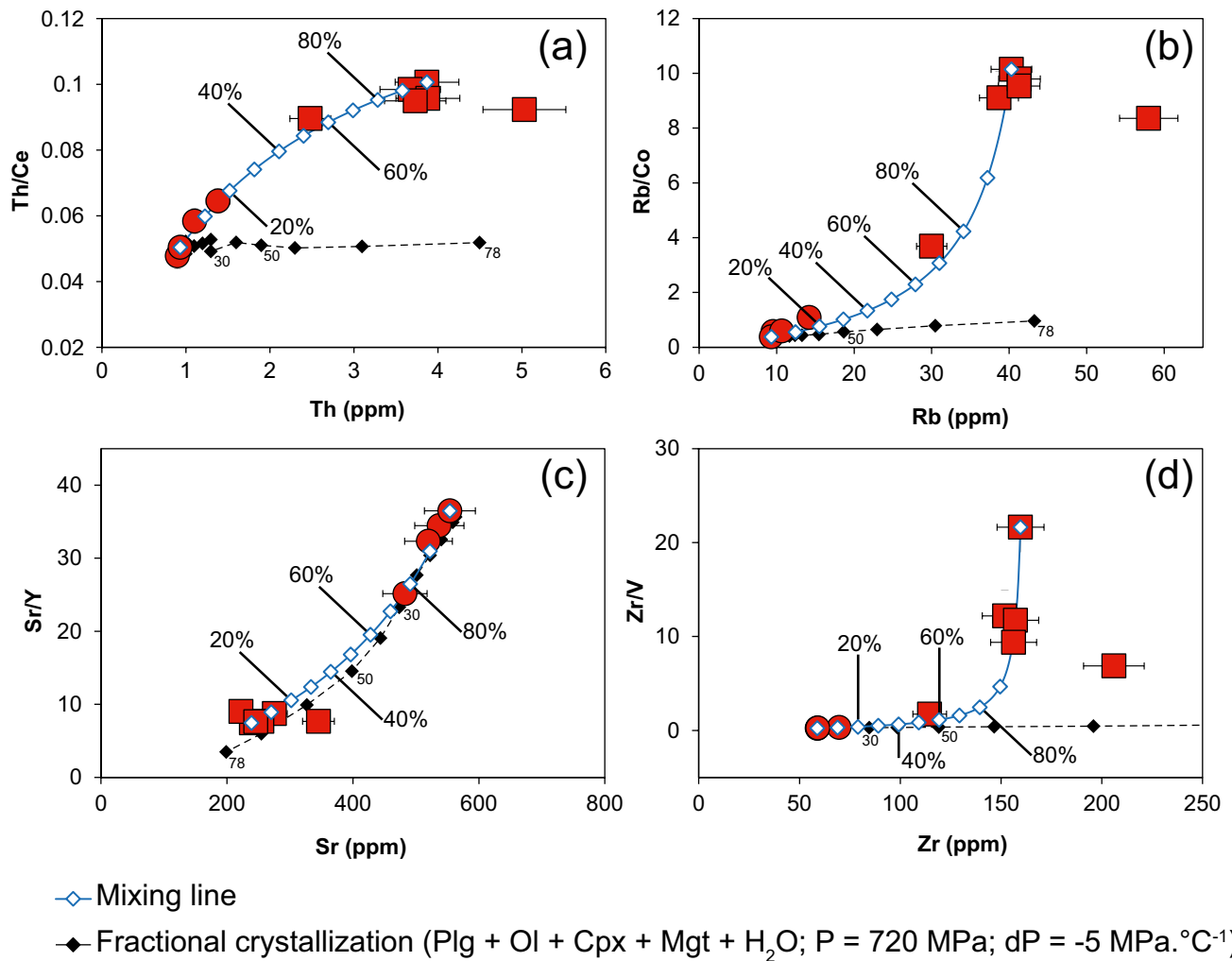


**Fig. 6** a–d Incompatible and compatible trace elements, with **a** Th/Ce versus Th, **b** Rb/Co versus Rb, **c** Sr/Y versus Sr, and **d** Zr/V versus Zr. The blue curve represents output of mixing calculation model (Gündüz and Asan 2021) between the most primitive and the most evolved measured MIs. The diamonds represent increment of 10% mixing by addition of the evolved end-member. The modeling fits very well with the measurements, supporting magma mixing as a main process in melt evolution. In contrast, modeled fractional crystallization (FC) paths (black dashed line) obtained using Petrolog3

(Danyushevsky and Plechov 2011) do not fit with the entire range of measured compositions, excepted in the case of Sr/Y versus Sr content. The black diamonds represent increments with steps of: 1% from 1 to 5% FC, 5% from 5 to 30% FC, and 10% from 30% to the end of the fractional crystallization. Distribution coefficients of the selected trace elements were obtained from LaTourrette and Burnett (1992), Hart and Dunn (1993), Forsythe et al. (1994), Bindeman et al. (1998), and Zanetti et al. (2004)

increases with differentiation (Fig. 4a), which is consistent with its incompatible behavior during differentiation. It ranges from 620 to 1118 ppm in olivine-hosted MIs and from 773 to 1439 ppm in pyroxene- and plagioclase-hosted MIs. Considering the Cl solubility in a hydrated magma (less than 1 wt.% Cl; Balcone-Boissard et al. 2016), the basaltic and andesitic melts of the Mocho-Choshuenco Enco eruption were undersaturated in Cl.

## Discussion

### Magmatic processes and storage conditions

The MI compositions permitted us to estimate their trapping temperature and pressure. In order to estimate MIs trapping temperatures, olivine-liquid thermometry was used for basaltic MIs. Equation 22 from Putirka (2008), considering

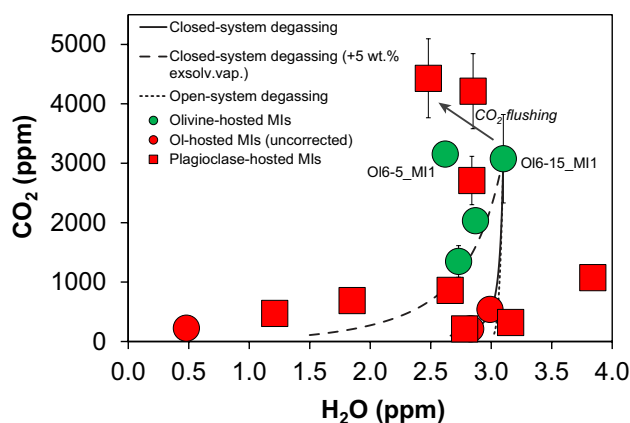


**Fig. 7** CO<sub>2</sub> vs. H<sub>2</sub>O contents diagram for the studied MIs. The green circles represent the corrected CO<sub>2</sub> content for the basaltic MIs Ol6-4\_MI1, Ol6-5\_MI1, Ol6-14\_MI1, and Ol6-15\_MI1. Closed-system (with and without vapor in excess) and open-system degassing paths starting from the composition of the CO<sub>2</sub>- and H<sub>2</sub>O-richest basaltic MI have been calculated using VolatileCalc (Newman and Lowenstern 2002). Most of data are well explained by degassing under closed-system conditions. In addition, the high CO<sub>2</sub> content measured in two plagioclase-hosted MIs suggests the occurrence of CO<sub>2</sub> flushing from depth. One sample (Pl2\_MI1, 3.84 wt. % H<sub>2</sub>O) is well outside this path and could be an indicator of a volatile-supersaturated melt (Pichavant et al. 2013)

hydrous conditions, yields temperatures of ~1050–1150 °C (note that the standard error of estimate (SEE) is 29 °C). It is well-known that water loss can occur due to H<sup>+</sup> diffusion through the host olivine (Chen et al. 2011). In the set of studied MIs, there is no clear evidence of post-entrapment water loss (except for Ol6-13\_MI1); however, we cannot exclude its occurrence. In this regard, lapilli smaller than 29 mm in size are expected to have similar cooling behavior to ash, with limited water loss (Lloyd et al. 2013). Thus, for the olivine-liquid thermometry, the calculation was based on all MIs except Ol6-13\_MI1. For andesitic and dacitic MIs, plagioclase-liquid thermometry, using Eq. 24a from Putirka (2008), yields temperatures of ~975–1095 °C (with SEE of 36 °C). Additionally, clinopyroxene-liquid thermometry, using the pressure-independent parametrization of Putirka et al. (1996), results in temperatures of ~1045–1105 °C (with SEE of 69 °C).

We estimated trapping pressure of the MIs using the models of Newman and Lowenstern (2002), Papale et al. (2006) and Witham et al. (2012) for basaltic MIs, and the experimental study of Botcharnikov et al. (2006) for andesitic melts. When considering this approach, loss of volatiles (H<sub>2</sub>O, CO<sub>2</sub>, S) from the melt into the bubble and/or to the host crystal must be taken into account. Diffusion of volatiles from the melt to the bubble can be important, as shown by Raman investigations (e.g., Esposito et al. 2016; Robidoux et al. 2018; Venugopal et al. 2020; Schiavi et al. 2020); therefore, the amounts measured in the glass are minimal

estimates. We calculated that a basaltic liquid containing 0.3 wt.% CO<sub>2</sub> and 3.0 wt.% H<sub>2</sub>O is in equilibrium with a fluid phase containing a mole fraction of H<sub>2</sub>O ≤ 0.1 at a temperature of 1100 °C and a pressure of 600 MPa. The very low amount of H<sub>2</sub>O that is predicted to be present inside the bubble would most likely be in the form of a very thin fluid film on the bubble wall (Venugopal et al. 2020), which may not be detected during the analyses, in agreement with our observations. Moreover, significant amounts of CO<sub>2</sub> and S can be stored in the bubble as mineral precipitates (carbonates, sulfides, or sulfates; Venugopal et al. 2020; Schiavi et al. 2020); thus, MIs volatile contents can be underestimated if their presence is neglected. Diffusion of volatiles from the melt to the bubble can partially explain the variability of CO<sub>2</sub> contents in the glass (Fig. 4d). Assuming melt saturation in both H<sub>2</sub>O and CO<sub>2</sub> and considering the inclusions with the highest volatile contents, we obtain the following trapping pressure range: 560–720 MPa (17–22 km depth) for the two most enriched basaltic olivine-hosted MIs (i.e., Ol6-15\_MI1 with 3077 ± 744 ppm CO<sub>2</sub> and Ol6-5\_MI1 with 3155 ± 190 ppm CO<sub>2</sub>) based on the corrected CO<sub>2</sub> content (melt + bubble, see Supplementary Material S2 for details on the correction calculations); 490 ± 10 MPa (14.5–15 km depth) for the andesitic plagioclase-hosted MIs (i.e., Pl1\_MI1 and Pl11\_MI1 with 4430 and 4213 ppm CO<sub>2</sub>, respectively). The latter is a minimal pressure estimate because the CO<sub>2</sub> content of the bubbles in plagioclase-hosted MIs is not known.

The major element compositions of MIs define two partially overlapping clusters: (1) with most olivine-hosted MIs being basaltic and representing parental magma and (2) plagioclase and pyroxene-hosted MIs (and olivine-hosted Ol6-12\_MI1) exhibiting more evolved compositions, i.e., mainly andesitic. The MI major element contents seem to follow a differentiation trend from the parental to the more evolved magma, with a compositional gap between the two groups of MIs. The presence of this compositional trend suggests that the two groups of MIs share the same origin. To investigate the role played by fractional crystallization, we modeled the evolution of melt compositions using Petrolog3 software (Danyushevsky and Plechov 2011). Details on the models selected are provided in Supplementary Material S5. The starting composition is defined by the less evolved MI composition (i.e., M16 MI), and starting pressure is fixed at 720 MPa, corresponding to the maximal estimated trapping pressure, while the starting temperature is fixed at 1100 °C. The water was treated incompatibly as the effect of CO<sub>2</sub> on H<sub>2</sub>O solubility is not taken into account in the models used. The two fractional crystallization models that better fit the major element data are shown in Fig. 3. In both models, the composition of the melt evolves by fractional crystallization of olivine, clinopyroxene, plagioclase, and magnetite in presence of H<sub>2</sub>O. The first model (1) set at

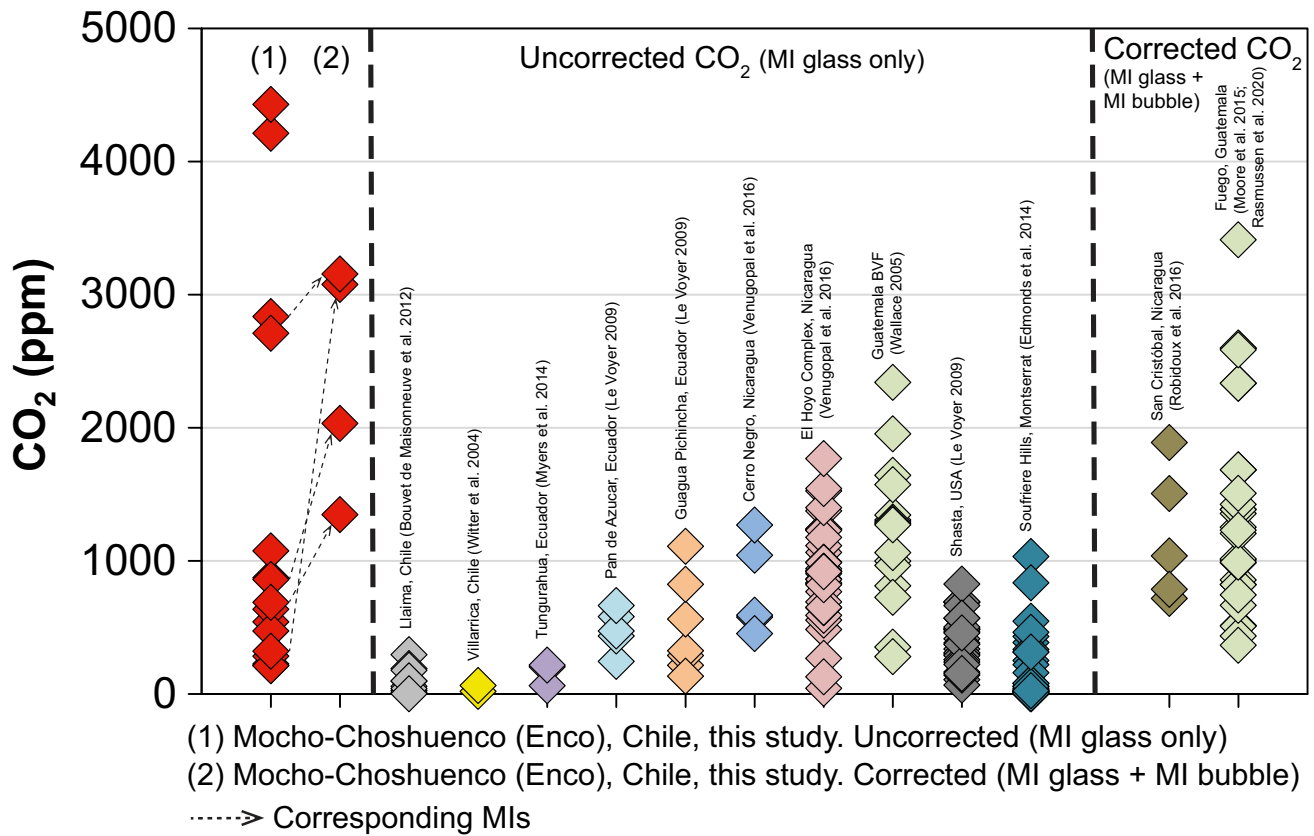


**Fig. 8** Comparison of CO<sub>2</sub> contents in MIs of the Enco magma (red diamonds on the left side of the diagram, showing exceptionally high contents) with data of other arc volcanic systems. The diagram shows studies giving “uncorrected” CO<sub>2</sub> contents (measured only in the MI

glass) and “corrected” CO<sub>2</sub> contents (i.e., taking into account the CO<sub>2</sub> content of both MI glass and bubble). The mean associated error with these data is ~15%

constant pressure ( $P = 720$  MPa) partially reproduces the compositional variability of the mafic olivine-hosted MIs but stops at 56% crystallization, due to depletion of TiO<sub>2</sub>, before reaching more evolved andesitic and dacitic compositions. Instead, the second model (2) of fractional crystallization associated to a fast decompression rate of the magma ( $-5$  MPa.°C<sup>-1</sup>) can reproduce the entire compositional range of major element data within about 75% of fractional crystallization. Despite the quite good fit obtained for the major element composition, fractional crystallization cannot be the only process responsible for the evolution from the basaltic end-member to the andesitic-dacitic one because of at least three main reasons. First, the final mineral compositions obtained in both models are not in agreement with the measured compositions in the investigated samples, i.e., Fo<sub>64</sub>-An<sub>61</sub>-En<sub>54</sub> and Fo<sub>45</sub>-An<sub>43</sub>-En<sub>27</sub> for models (1) and (2), respectively, against measured mineral compositions of Fo<sub>75-81</sub>-An<sub>44-51</sub>/An<sub>76</sub>-En<sub>42-67</sub>. Possibly, as a significant CO<sub>2</sub> content in the melt and the presence (rare) of orthopyroxene in the investigated samples are not considered in the models used, the accuracy of the output may be low. Thus, some care should be taken with these modeling results. Second,

simple calculations demonstrate that variations in absolute trace element concentrations as well as in trace element ratios (Fig. 6) cannot be explained by a process of fractional crystallization alone. A good fit is only observed for Sr/Y versus Sr contents (Fig. 6c), probably due to the fact that Sr has a compatible behavior with plagioclase (Bindeman et al. 1998). Instead, fractional crystallization can partially account for the compositional variability (major and trace elements) of the olivine-hosted basaltic melts. Third, as the mafic and evolved end-members in the MIs were co-erupted, it is not likely that they were directly related by only fractional crystallization, with the host minerals being most probably phenocrysts. In fact, physical models taking into account the evolution of parameters such as magma density, viscosity, and crystal nucleation/growth rates (Brophy 2009) cannot explain the occurrence of an extreme degree of fractional crystallization (i.e., up to 75%) coupled to rapid magma ascent.

We consider trace elements to assess if the observed compositional trends are the result of a process of magma mixing. In the case of major elements, mixing lines between averaged compositions of olivine-hosted MIs and

plagioclase/pyroxene-hosted MIs were calculated (but not shown in Fig. 3 for clarity) and may explain the clusters observed. However, as fractional crystallization possibly occurs, especially in the case of basaltic melts, major elements do not show well-defined linear trends. PetroGram (Gündüz and Asan 2021) was used to model magma mixing for trace elements (Fig. 6). Highly to moderately incompatible elements like Th, Rb, Ce, Y, and Zr have low mineral-melt partition coefficients, while Sr is compatible in plagioclase, Co has strong affinity with olivine (and to a lesser extent, clinopyroxene), and V is slightly incompatible in clinopyroxene under slightly oxidizing conditions (e.g., see Laubier et al. 2014; Geochemical Earth Reference Model 2018). The magma mixing appears as a hyperbolic curve in incompatible/incompatible or incompatible/compatible versus incompatible trace element plots (Fig. 6). Incremental mixing from the most primitive melt measured (O16-14\_MI1) to the most evolved end-member (represented by P15\_MI1 sample) reproduces successfully trace element data. At the scale of the lapilli, mingling-like textures were observed with clearer portions in contact with darker portions. Thus, the compilation of sample observations, major, trace element data, and modeling suggests that the Enco eruption occurred as a result of mixing between a hot basaltic magma (represented by olivine-hosted MIs), which was evolving by fractional crystallization at depth, and a colder, more evolved, andesitic to dacitic magma (represented by plagioclase and pyroxene-hosted MIs).

### Volatiles in the Enco magma

The different textures in the MIs reflect various formation and/or post-entrapment processes. While the majority of the analyzed MIs show a regular shape and exhibit only one shrinkage bubble, the olivine-hosted inclusion O16-13\_MI1 with a single large bubble (Fig. 2b) has the lowest water (0.48 wt.%) and CO<sub>2</sub> (225 ppm) contents, which suggest fast decompression of the inclusion (depressurization and then vesiculation or decrepitation) (Lowenstern 1995), and important volatiles loss. Among the studied inclusions, the olivine-hosted inclusion O16-5\_MI1 (Fig. 7) has the highest measured CO<sub>2</sub> content in the glass (2836 ppm) and the highest corrected total (glass + bubble) CO<sub>2</sub> concentration of  $3155 \pm 190$  ppm for this mineral phase. However, when taking into account the correction uncertainty, the inclusion O16-15\_MI1 may display the highest corrected CO<sub>2</sub> content with  $3077 \pm 744$  ppm. Higher CO<sub>2</sub> contents have been measured in plagioclase-hosted MIs with up to 4430 ppm in P1M1\_MI1 (uncorrected data, glass content only). A peculiar texture has been observed in this sample and also in O16-5\_MI1 (Fig. 2c), O16-4\_MI1, and P12\_MI1, with numerous small bubbles evenly distributed that suggest fast exsolution of the volatiles and quenching of the

small bubbles hence formed. The presence of a large number of very small bubbles preserved in the glass of several inclusions indicates volatile supersaturation causing a high nucleation rate and is possible evidence of a very rapid syn-eruptive decompression followed by rapid quench, as shown by theory and experimental results (Mourtada-Bonnefoi and Laporte 2004; Toramaru 2006; Le Gall and Pichavant 2016). It is worth noting that the two olivine-hosted MIs showing this texture are those with the highest CO<sub>2</sub> contents in the glass, whereas high CO<sub>2</sub> concentration in the glass is not systematically associated to a large number of bubbles in plagioclase-hosted MIs. Moreover, both textures (i.e., bubble-rich, and single bubble) are observed in the same tephra unit. These observations can be explained by the high sensitivity of bubble nucleation to small variations in initial conditions (e.g., Mourtada-Bonnefoi and Laporte 2004; Toramaru 2006; Le Gall and Pichavant 2016), including the internal pressure and volatile concentration in the melt, but also to post-entrapment crystallization processes, thermal contraction, and elastic deformation (volumetric re-equilibration) (Schiavi et al. 2016; Drignon et al. 2020) that affect MIs before quenching.

An early degassing before the MIs entrapment could explain the large variability of CO<sub>2</sub>, H<sub>2</sub>O, and S contents observed at a given K<sub>2</sub>O value (Fig. 4). Additionally, mixing between the mafic magma and the andesitic-dacitic one is able to affect the volatile contents, as observed in the case of S (Fig. 4b). Most data plotted in the CO<sub>2</sub> vs. H<sub>2</sub>O contents diagram (Fig. 7) can be explained by a closed-system equilibrium degassing of the melt in presence of excess vapor. This is consistent with the strong explosivity behavior observed for the Enco eruption, as a closed-system equilibrium degassing would keep the volatiles under pressure (see also, Cassidy et al. 2018). The high CO<sub>2</sub> content measured in some MIs, in particular in two plagioclase-hosted MIs, also suggests the occurrence of CO<sub>2</sub> flushing from depth, as observed in several other volcanic systems (Blundy et al. 2010). We do not have a clear explanation for the high H<sub>2</sub>O content (3.84 wt.%) of the inclusion P12\_MI1 hosted in the Ca-rich plagioclase (An<sub>76</sub>) that plots above the main trend, but we cannot exclude the possibility that it is a previously formed xenocryst or that it registered supersaturation of the magma in a deep portion of the system (Pichavant et al. 2013).

The H<sub>2</sub>O, S, and Cl contents of the Enco magma are within the ranges given for other arc volcanic systems (Wallace 2005). The CO<sub>2</sub> contents in some of our MIs, however, are exceptionally high (up to 4430 ppm in the glass of P1M1\_MI1, Table 1). The four most enriched MIs have CO<sub>2</sub> contents higher than those given by studies on other arc volcanoes in South and Central America (generally no more than 2000 ppm; see Fig. 8). In those studies, CO<sub>2</sub> in the bubbles was generally not taken into account. Two exceptions



are the MIs from San Cristobal (Nicaragua), for which corrected CO<sub>2</sub> contents are 718–1889 ppm versus 71–527 ppm for uncorrected data (Robidoux et al. 2016), and the MIs from Fuego (Guatemala) with corrected CO<sub>2</sub> contents of 513–2598 ppm versus 189–511 ppm for uncorrected data (Moore et al. 2015). Recent work by Rasmussen et al. (2020) gave corrected CO<sub>2</sub> contents for Fuego (Guatemala) ranging from 370 to 3409 ppm.

A possible mechanism of CO<sub>2</sub> enrichment at upper levels could be a gas flushing event (Caricchi et al. 2018), which seems in agreement with our observations (Fig. 7). According to the trace elements analysis, the magma of the Enco eruption of Mocho-Choshuenco volcano derived from a mixing between a deep and primitive basaltic magma rising from more than 22 km in depth and an evolved andesitic to dacitic magma stored in a hypothetical, shallower reservoir at a minimum estimated depth of 15 km. These estimates, as already stated previously, are minimal. However, only few studies in the literature report the composition of magmas erupted at Mocho-Choshuenco volcano. Moreover, no geophysical study, showing the position of a magmatic reservoir is, until now, available at Mocho-Choshuenco in order to confirm the minimal depth estimates obtained with MI investigations. Thus, our data are also important in providing this first vital information for future investigations that will better define magma storage conditions below Mocho-Choshuenco. The recharge of the magma chamber by this primitive CO<sub>2</sub>-rich magma has possibly resulted in the enrichment in CO<sub>2</sub> and the triggering of the eruption. Hence, the high CO<sub>2</sub> content could have been the main cause of the explosivity of the Enco eruption event that generated highly mobile pyroclastic flows. In fact, other possible causes of explosivity seem not significant. The high temperature (> 1000 °C) and the low crystallinity (< 30 vol.%, including macrocysts and microliths) of the erupted magma both suggest that the magma had a low viscosity and was not prone to an explosive regime (Lavallée et al. 2007). From the model of Vetere et al. (2006) for andesitic melts, with a water content of ~ 3.0 wt.%, the viscosity of the magma that fed the Enco eruption is estimated to be ~ 10<sup>2</sup>–10<sup>3</sup> Pa.s, which is in the low viscosity range, while the high viscosity range is between 10<sup>8</sup> and 10<sup>13</sup> Pa.s (Vetere et al. 2006). As a comparison, the range of viscosities estimated at Mocho-Choshuenco for the Enco eruption is at least three orders of magnitude lower than the effusive eruption of Quizapu volcano (Chile), which emitted a 5 km<sup>3</sup> andesitic-dacitic mingled lava flow in A.D. 1846–1847, with pre-eruptive H<sub>2</sub>O contents of ~ 4–6 wt.% (Ruprecht and Bachmann 2010). The effusive behavior of this eruption, despite the relatively high viscosity of its magma, was explained by a late reheating following a mixing of dacite with andesite recharge;

leading to an acceleration of volatile diffusion; enhancing bubble nucleation, growth, and coalescence; and inhibiting brittle fragmentation (Ruprecht and Bachmann 2010). In the case of the Quizapu, the andesitic-dacitic mixing has prevented an explosive eruption to occur; as generally, silicic magma explosivity is strongly controlled by the viscosity (Cassidy et al. 2018). In contrast, the magma mixing which occurred at Mocho-Choshuenco seems to have rather favored the overpressure, possibly due to the high CO<sub>2</sub> contents, leading to the sub-Plinian Enco eruption. The CO<sub>2</sub> contents measured at Mocho-Choshuenco are also significantly higher than those recorded in some other Chilean volcanoes such as Llaima or Villarica, with CO<sub>2</sub> contents measured in MI glass below 500 ppm (see Fig. 8; Witter et al. 2004; Bouvet de Maisonneuve et al. 2012).

Finally, H<sub>2</sub>O, S, and Cl contents are within the range of other arc volcanic systems around the world, with no exceptional concentrations measured (Wallace 2005). In this context, the low solubility of CO<sub>2</sub> (Bottinga and Javoy 1990; Le Gall and Pichavant 2016; Laporte et al. 2016) could have controlled the eruption dynamics. Moreover, CO<sub>2</sub> is known to significantly decrease the solubility of H<sub>2</sub>O (Lowenstern 2001 and references therein). Water contents are also high; hence, high amounts of exsolved volatiles (CO<sub>2</sub> and H<sub>2</sub>O) could have increased the magma buoyancy, generated high overpressures, and favored fast ascent of the magma and explosive fragmentation (Papale and Polacci 1999; Blundy et al. 2010; Freda et al. 2010; Aiuppa et al. 2011; Dallai et al. 2011; Allison et al. 2021). Owing to the exceptionally high CO<sub>2</sub> and fairly high H<sub>2</sub>O contents we report, it appears that the magma of the Enco-MC15 eruption at Mocho-Choshuenco was particularly prone to explode violently despite its moderate silica content.

## Conclusions

We measured the volatile contents of MIs in minerals extracted from juveniles of a pyroclastic flow deposit formed during the andesitic Enco-MC15 eruption of Mocho-Choshuenco volcano. Though H<sub>2</sub>O, S, and Cl contents are in ranges given for other arc volcanic systems, the CO<sub>2</sub> contents are exceptionally high compared to those given in published studies, with concentrations up to 4430 ppm. The initial CO<sub>2</sub> content was probably even higher, as suggested by the MI textures (i.e., presence of hundreds of small bubbles) as well as precipitated carbonates inside shrinkage bubbles. 3D Raman mapping allowed us to quantify the volume of solid carbonates trapped in inclusion bubbles and, thus, correct the CO<sub>2</sub> content in the MIs. As a whole, the volatile contents indicate that the basaltic MIs hosted in olivines were trapped at minimal depths of ~ 17–22 km, whereas trapping

of andesitic to dacitic melts in plagioclase crystals occurred at ~ 15 km depth.

We conclude that the exceptionally high content and the low solubility of CO<sub>2</sub>, combined with the fact that this volatile phase enhanced exsolution of H<sub>2</sub>O, could have caused high overpressure in the magma reservoir and led the crystal-poor Enco andesitic magma of low viscosity to erupt explosively. A possible scenario considers that the deeper basaltic CO<sub>2</sub>-rich magma ascended and recharged a shallower reservoir where the andesitic-dacitic magma was ponding. Once there, the mafic magma began to cool, exsolved volatiles, and mixed with the evolved magma, which resulted in rising of gas pressure (similar to gas sparging of Bachmann and Bergantz 2006); possible rapid bubble expansion associated with fast magma ascent finally triggered the explosive eruption. We note that the wide range of glass compositions and textures (i.e., scarce presence of phenocrysts and microliths, hundreds of bubbles preserved in the inclusion glass) of the studied samples seem to testify to a mild mixing process associated with a very rapid ascent of the recharging magma through the shallower storage levels, most likely caused by the strong enrichment in CO<sub>2</sub> of the basaltic melt. Further investigations on other explosive eruptions of Mocho-Choshueno volcano are needed to confirm if the CO<sub>2</sub> enrichment is a typical feature throughout the life of the edifice or if it concerned only the Enco eruption. Our study supports the conclusions of earlier works that pointed out the possible correlation between high CO<sub>2</sub> contents and explosivity of poorly to moderately differentiated magmas. It suggests also that initial CO<sub>2</sub> contents in arc magmas may be commonly underestimated and that further work is required to better constrain the role that CO<sub>2</sub> may have in promoting explosive eruptions of basic to intermediate magmas.

**Supplementary Information** The online version contains supplementary material available at <https://doi.org/10.1007/s00445-022-01550-y>.

**Acknowledgements** The authors thank the Associate Editor, Tobias Fischer, as well as Tom Shea, and an anonymous reviewers for their constructive and helpful reviews. We thank Jean-Luc Devidal (LMV) for assistance with the electron microprobe and LA-ICP-MS and Etienne Deloule for his help with the ion probe at CRPG Nancy.

**Funding** Open access funding provided by University of Vienna. This research was financed by the French National Research Institute for sustainable Development (IRD), the French Government Laboratory of Excellence initiative No. ANR-10-LABX-0006, the Region Auvergne and the European Regional Development Fund, and the Chilean Science Commission (Fondecyt projects 1070162 and 1090387). This is Laboratory of Excellence ClerVolc contribution number 533.

**Open Access** This article is licensed under a Creative Commons Attribution 4.0 International License, which permits use, sharing, adaptation, distribution and reproduction in any medium or format, as long as you give appropriate credit to the original author(s) and the source, provide a link to the Creative Commons licence, and indicate if changes were made. The images or other third party material in this article are

included in the article's Creative Commons licence, unless indicated otherwise in a credit line to the material. If material is not included in the article's Creative Commons licence and your intended use is not permitted by statutory regulation or exceeds the permitted use, you will need to obtain permission directly from the copyright holder. To view a copy of this licence, visit <http://creativecommons.org/licenses/by/4.0/>.

## References

- Aiuppa A, Burton M, Allard P, Caltabiano T, Giudice G, Gurrieri S, Liuzzo M, Salerno G (2011) First observational evidence for the CO<sub>2</sub>-driven origin of Stromboli's major explosions. *Solid Earth* 2(2):135–142. <https://doi.org/10.5194/se-2-135-2011>
- Allison CM, Roggensack K, Clarke AB (2021) Highly explosive basaltic eruptions driven by CO<sub>2</sub> exsolution. *Nat Commun* 12:217. <https://doi.org/10.1038/s41467-020-20354-2>
- Anderson AT, Brown GG (1993) CO<sub>2</sub> contents and formation pressures of some Kilauean melt inclusions. *Am Mineral* 78(7–8):794–803
- Bachmann O, Bergantz GW (2006) Gas percolation in upper-crustal silicic crystal mushes as a mechanism for upward heat advection and rejuvenation of near-solidus magma bodies. *J Volcanol Geotherm Res* 149(1–2):85–102. <https://doi.org/10.1016/j.jvolgeoes.2005.06.002>
- Balcone-Boissard H, Boudon G, Cioni R, Webster JD, Zdanowicz G, Orsi G, Civetta L (2016) Chlorine as a geobarometer for alkaline magmas: evidence from a systematic study of the eruptions of Mount Somma-Vesuvius. *Sci Rep* 6:21726. <https://doi.org/10.1038/srep21726>
- Bindeman IN, Davis AM, Drake MJ (1998) Ion microprobe study of plagioclase-basalt partition experiments at natural concentration levels of trace elements. *Geochim Cosmochim Acta* 62(7):1175–1193. [https://doi.org/10.1016/S0016-7037\(98\)00047-7](https://doi.org/10.1016/S0016-7037(98)00047-7)
- Blundy J, Cashman KV, Rust A, Witham F (2010) A case for CO<sub>2</sub>-rich arc magmas. *Earth Planet Sci Lett* 290(3–4):289–301. <https://doi.org/10.1016/j.epsl.2009.12.013>
- Botcharnikov RE, Behrens H, Holtz F (2006) Solubility and speciation of C-O-H fluids in andesitic melt at T = 1100–1300 °C and P = 200 and 500 MPa. *Chem Geol* 229(1–3):125–143. <https://doi.org/10.1016/j.chemgeo.2006.01.016>
- Bottinga Y, Javoy M (1990) MORB degassing: bubble growth and ascent. *Chem Geol* 81(4):255–270. [https://doi.org/10.1016/0009-2541\(90\)90050-H](https://doi.org/10.1016/0009-2541(90)90050-H)
- Bouvet de Maisonneuve C, Dungan MA, Bachmann O, Burgisser A (2012) Insights into shallow magma storage and crystallization at Volcan Llaima (Andean Southern Volcanic Zone, Chile). *J Volcanol Geotherm Res* 211–212:76–91. <https://doi.org/10.1016/j.jvolgeoes.2011.09.010>
- Brophy JG (2009) Decompression and H<sub>2</sub>O exsolution driven crystallization and fractionation: development of a new model for low-pressure fractional crystallization in calc-alkaline magmatic systems. *Contrib Mineral Petrol* 157:797–811. <https://doi.org/10.1007/s00410-008-0365-2>
- Caricchi L, Sheldrake TE, Blundy J (2018) Modulation of magmatic processes by CO<sub>2</sub> flushing. *Earth Planet Sci Lett* 491:160–171. <https://doi.org/10.1016/j.epsl.2018.03.042>
- Cassidy M, Manga M, Cashman K, Bachmann O (2018) Controls on explosive-effusive volcanic eruption styles. *Nat Commun* 9:2839. <https://doi.org/10.1038/s41467-018-05293-3>
- Chen Y, Provost A, Schiano P, Cluzel N (2011) The rate of water loss from olivine-hosted melt inclusions. *Contrib Mineral Petrol* 162:625–636. <https://doi.org/10.1007/s00410-011-0616-5>
- Clavero J, Roche O, Rivera A (2008) Recent unusual fines-depleted and highly-mobile andesitic pyroclastic flows from

- Mocho-Choshuenco volcano, southern Andes. IAVCEI General Assembly, August 18–25, Reykjavik, Iceland.
- Coltelli M, Del Carlo P, Vezzoli L (1998) Discovery of a Plinian basaltic eruption of Roman age at Etna volcano. *Italy Geology* 26(12):1095–1098. [https://doi.org/10.1130/0091-7613\(1998\)026%3c1095:DOAPBE%3e2.3.CO;2](https://doi.org/10.1130/0091-7613(1998)026%3c1095:DOAPBE%3e2.3.CO;2)
- Costa F, Andreastuti S, Bouvet de Maisonneuve C, Pallister JS (2013) Petrological insights into the storage conditions, and magmatic processes that yielded the centennial 2010 Merapi explosive eruption. *J Volcanol Geotherm Res* 261:209–235. <https://doi.org/10.1016/j.jvolgeores.2012.12.025>
- Cross JK, Tomlinson EI, Giordano G, Smith VC, De Benedetti AA, Roberge J, Manning CJ, Wulf S, Menzies MA (2014) High level triggers for explosive mafic volcanism: Albano Maar, Italy. *Lithos* 190–191:137–153. <https://doi.org/10.1016/j.lithos.2013.11.001>
- Dallai L, Cioni R, Boschi C, D’Orlando C (2011) Carbonate-derived CO<sub>2</sub> purging magma at depth: influence on the eruptive activity of Somma-Vesuvius. *Italy Earth Planet Sci Lett* 310(1–2):84–95. <https://doi.org/10.1016/j.epsl.2011.07.013>
- Danyushevsky LV, Plechov P (2011) Petrolog3: integrated software for modeling crystallization processes. *Geochemi Geophys Geosys* 12(7):Q07021. <https://doi.org/10.1029/2011GC003516>
- Deegan FM, Troll VR, Freda C, Misiti V, Chadwick JP, McLeod CL, Davidson JP (2010) Magma–carbonate interaction processes and associated CO<sub>2</sub> release at Merapi volcano, Indonesia: insights from experimental petrology. *J Petrol* 51:1027–1051. <https://doi.org/10.1093/ptrology/egq010>
- Drignon MJ, Arbaret L, Cluzel N, Nielsen RL, Bodnar RJ (2020) Experimentally induced volumetric re-equilibration of plagiocles-hosted melt inclusions. *Geochem Geophys Geosyst* 22(1):2020GC009357. <https://doi.org/10.1029/2020GC009357>
- Edmonds M, Humphreys MC, Hauri EH, Herd RA, Wadge G, Rawson H, Ledden R, Plail M, Barclay J, Aiuppa A (2014) Pre-eruptive vapour and its role in controlling eruption style and longevity at Soufrière Hills Volcano. In: Wadge G, Robertson REA, Voight B (eds.) *The Eruption of Soufrière Hills Volcano, Montserrat from 2000 to 2010*, Geological Society, London, *Memoirs*, 39, pp. 291–315. <https://doi.org/10.1144/M39.16>
- Esposito R, Lamadrid HM, Redi D, Steele-MacInnis M, Bodnar RJ, Manning CE, De Vivo B, Cannatelli C, Lima A (2016) Detection of liquid H<sub>2</sub>O in vapour bubbles in reheated melt inclusions: implications for magmatic fluid composition and volatile budgets of magmas? *Am Mineral* 101:1691–1695. <https://doi.org/10.2138/am-2016-5689>
- Fontijn K, Rawson H, Van Daele M, Moernaut J, Abarzúa AM, Heirman K, Bertrand S, Pyle DM, Mather TA, De Batist M, Naranjo JA, Moreno H (2016) Synchronisation of sedimentary records using tephra: a postglacial tephrochronological model for the Chilean Lake District. *Quat Sci Rev* 137:234–254. <https://doi.org/10.1016/j.quascirev.2016.02.015>
- Forsythe LM, Nielsen RL, Fisk MR (1994) High-field-strength element partitioning between pyroxene and basaltic to dacitic magmas. *Chem Geol* 117:107–125. [https://doi.org/10.1016/0009-2541\(94\)90124-4](https://doi.org/10.1016/0009-2541(94)90124-4)
- Freda C, Gaeta M, Giaccio B, Marra F, Palladino DM, Scarlato P, Sottili G (2010) CO<sub>2</sub>-driven large mafic explosive eruptions: the Pozzolane Rosse case study from the Colli Albani Volcanic District (Italy). *Bull Volcanol* 73(3):241–256. <https://doi.org/10.1007/s00445-010-0406-3>
- Frezzotti ML, Tecce F, Casagli A (2012) Raman spectroscopy for fluid inclusion analysis. *J Geochem Explor* 112:1–20. <https://doi.org/10.1016/j.gexplo.2011.09.009>
- Gardner JE (2009) The impact of pre-existing gas on the ascent of explosively erupted magma. *Bull Volcanol* 71:835–844. <https://doi.org/10.1007/s00445-009-0276-8>
- Geochemical Earth Reference Model (GERM) Partition Coefficient (Kd) Database (2018) <https://earthref.org/KDD/> (accessed 20<sup>th</sup> March 2018)
- Gonnermann HM, Manga M (2007) The fluid mechanics inside a volcano. *Annu Rev Fluid Mech* 39:321–356. <https://doi.org/10.1146/annurev.fluid.39.050905.110207>
- Gündüz M, Asan K (2021) PetroGram: an Excel-based petrology program for modeling of magmatic processes. *Geosci Front* 12(1):81–92. <https://doi.org/10.1016/j.gsf.2020.06.010>
- Hart SR, Dunn T (1993) Experimental cpx/melt partitioning of 24 trace elements. *Contrib Mineral Petrol* 113:1–8. <https://doi.org/10.1007/BF00320827>
- Houghton BF, Wilson CJN, Del Carlo P, Catelli M, Sable JE, Carey JR (2004) The influence of conduit processes on changes in style of basaltic Plinian eruptions: Tarawera 1886 and Etna 122 BC. *J Volcanol Geotherm Res* 137(1–3):1–14. <https://doi.org/10.1016/j.jvolgeores.2004.05.009>
- Huppert HE, Woods AW (2002) The role of volatiles in magma chamber dynamics. *Nature* 420(6915):493–495. <https://doi.org/10.1038/nature01211>
- Jugo P (2009) Sulfur content at sulfide saturation in oxidized magmas. *Geology* 37 (5):415–418. <https://doi.org/10.1130/G25527A.1>
- Lamadrid HM, Moore LR, Moncada D, Rimstidt JD, Burruss RC, Bodnar RJ (2017) Reassessment of the Raman CO<sub>2</sub> densimeter. *Chem Geol* 450:210–222. <https://doi.org/10.1016/j.chemgeo.2016.12.034>
- Laporte D, Hardiagon M, Provost A (2016) Ascent and degassing of magmas: the conditions of homogeneous bubble nucleation in the system basalt-CO<sub>2</sub>. *Experimental Mineralogy, Petrology and Geochemistry, EMPG XV - International Conference, Zürich, Switzerland, June 5–8, 2016*.
- LaTourrette TZ, Burnett DS (1992) Experimental determination of U and Th partitioning between clinopyroxene and natural and synthetic basaltic liquid. *Earth Planet Sci Lett* 110:227–244. [https://doi.org/10.1016/0012-821X\(92\)90050-6](https://doi.org/10.1016/0012-821X(92)90050-6)
- Laubier M, Grove TL, Langmuir CH (2014) Trace element mineral/melt partitioning for basaltic and basaltic andesitic melts: an experimental and laser ICP-MS study with application to the oxidation state of mantle source regions. *Earth Planet Sci Lett* 392:265–278. <https://doi.org/10.1016/j.epsl.2014.01.053>
- Lavallée Y, Hess KU, Cordonnier B, Dingwell DB (2007) Non-Newtonian law for highly crystalline dome lavas. *Geology* 35(9):843–846. <https://doi.org/10.1130/G23594A.1>
- Le Gall N, Pichavant M (2016) Homogeneous bubble nucleation in H<sub>2</sub>O- and H<sub>2</sub>O-CO<sub>2</sub>-bearing basaltic melts: results of high temperature decompression experiments. *J Volcanol Geotherm Res* 327:604–621. <https://doi.org/10.1016/j.jvolgeores.2016.10.004>
- Le Voyer M (2009) *Rôle des fluides dans la genèse des magmas d’arc: analyses in-situ des éléments volatils et des isotopes du bore dans les inclusions magmatiques des olivines primitives*. PhD Thesis, Geochemistry, Université Blaise Pascal, Clermont-Ferrand II, France, 276p. <https://tel.archives-ouvertes.fr/tel-00453889>
- Le Voyer M, Kelley KA, Cottrell E, Hauri EH (2017) Heterogeneity in mantle carbon content from CO<sub>2</sub>-undersaturated basalts. *Nat Commu* 8:14062. <https://doi.org/10.1038/ncomms14062>
- Lesne P, Scaillet B, Pichavant M (2015) The solubility of sulfur in hydrous basaltic melts. *Chem Geol* 418:104–116. <https://doi.org/10.1016/j.chemgeo.2015.03.025>
- Lloyd AS, Plank T, Ruprecht P, Hauri E, Rose W (2013) Volatile loss from melt inclusions in pyroclasts of differing sizes. *Contrib Mineral Petrol* 165(1):129–153. <https://doi.org/10.1007/s00410-012-0800-2>
- Lowenstern JB (1995) Application of silicate-melt inclusions to the study of magmatic volatiles. In: Thompson JFH (ed.) *Magmas, Fluids and Ore Deposits*. Mineralogical Association of Canada, pp. 71–100.

- Lowenstern JB (2001) Carbon dioxide in magmas and implications for hydrothermal systems. *Miner Deposita* 36(6):490–502. <https://doi.org/10.1007/s001260100185>
- McPhie J (1990) Phreatomagmatic and phreatic fall and surge deposits from explosions at Kilauea Volcano, Hawaii, 1790 A.D. Keanakāko'i Ash Member. *Bull Volcanol.* 52(5):334–354. <https://doi.org/10.1007/BF00302047>
- Métrich N, Clocchiatti R (1996) Sulfur abundance and its speciation in oxidized alkaline melts. *Geochim Cosmochim Acta* 60:4151–4160. [https://doi.org/10.1016/S0016-7037\(96\)00229-3](https://doi.org/10.1016/S0016-7037(96)00229-3)
- Métrich N, Allard P, Spilliaert N, Andronico D, Burton M (2004) 2001 flank eruption of the alkali- and volatile-rich primitive basalt responsible for Mount Etna's evolution in the last three decades. *Earth Planet Sci Lett* 228:1–17. <https://doi.org/10.1016/j.epsl.2004.09.036>
- Moore L, Gazel E, Tuohy R, Lloyd A, Esposito R, Steele-MacInnis M, Hauri EH, Wallace PJ, Plank T, Bodnar RJ (2015) Bubbles matter: an assessment of the contribution of vapor bubbles to melt inclusion volatile budgets. *Am Mineral* 100(4):806–823. <https://doi.org/10.2138/am-2015-5036>
- Moreno H, Lara L (2007) Geología del Complejo Volcánico Mocho-Choshuenco, Carta Geológica de Chile. Serie Geología Básica 107:1–27
- Moretti R, Métrich N, Arienzo I, Di Renzo V, Aiuppa A, Allard P (2018) Degassing vs. eruptive styles at Mt. Etna volcano (Sicily, Italy). Part I: Volatile stocking, gas fluxing, and the shift from low-energy to highly explosive basaltic eruptions. *Chem Geol* 482:1–17. <https://doi.org/10.1016/j.chemgeo.2017.09.017>
- Moune S, Sigmarsson O, Schiano P, Thordarson T, Keiding JK (2012) Melt inclusion constraints on the magma source of Eyjafjallajökull 2010 flank eruption. *J Geophys Res-Solid Earth* 117:B00C07. <https://doi.org/10.1029/2011JB008718>
- Mourtada-Bonnefoi CC, Laporte D (2004) Kinetics of bubble nucleation in a rhyolitic melt: an experimental study of the effect of ascent rate. *Earth Planet Sci Lett* 218(3–4):521–537. [https://doi.org/10.1016/S0012-821X\(03\)00684-8](https://doi.org/10.1016/S0012-821X(03)00684-8)
- Myers ML, Geist DJ, Rowe MC, Harpp KS, Wallace PJ, Dufek J (2014) Replenishment of volatile-rich mafic magma into a degassed chamber drives mixing and eruption of Tungurahua Volcano. *Bull Volcanol* 76(11):1–17. <https://doi.org/10.1007/s00445-014-0872-0>
- Newman S, Lowenstern JB (2002) VolatileCalc: a silicate melt-H<sub>2</sub>O-CO<sub>2</sub> solution model written in visual basic for Excel. *Comput and Geosci* 28(5):597–604. [https://doi.org/10.1016/S0098-3004\(01\)00081-4](https://doi.org/10.1016/S0098-3004(01)00081-4)
- Papale P, Polacci M (1999) Role of carbon dioxide in the dynamics of magma ascent in explosive eruptions. *Bull Volcanol* 60(8):583–594. <https://doi.org/10.1007/s004450050253>
- Papale P, Moretti R, Barbato D (2006) The compositional dependence of the saturation surface of H<sub>2</sub>O+CO<sub>2</sub> fluids in silicate melts. *Chem Geol* 229(1):78–95. <https://doi.org/10.1016/j.chemgeo.2006.01.013>
- Pichavant M, Di Carlo I, Rotolo SG, Scaillet B, Burgisser A, Le Gall N, Martel C (2013) Generation of CO<sub>2</sub>-rich melts during basalt magma ascent and degassing. *Contrib Mineral Petrol* 166:545–561. <https://doi.org/10.1007/s00410-013-0890-5>
- Putirka KD (2008) Thermometers and barometers for volcanic systems. *Rev Mineral Geochem* 69(1):61–120. <https://doi.org/10.2138/rmg.2008.69.3>
- Putirka K, Johnson M, Kinzler R, Walker D (1996) Thermobarometry of mafic igneous rocks based on clinopyroxene-liquid equilibria, 0–30 kbar. *Contrib Mineral Petrol* 123:92–108. <https://doi.org/10.1007/s004100050145>
- Ramsey CB (2009) Dealing with outliers and offsets in radiocarbon dating. *Radiocarbon* 51(3):1023–1045. <https://doi.org/10.1017/S0033822200034093>
- Rasmussen DJ, Plank TA, Wallace PJ, Newcombe ME, Lowenstern JB (2020) Vapor-bubble growth in olivine-hosted melt inclusions. *Am Min* 105:1898–1919. <https://doi.org/10.2138/am-2020-7377>
- Rawson H, Naranjo JA, Smith V, Fontijn K, Pyle DM, Mather TA, Moreno H (2015) The frequency and magnitude of post-glacial explosive eruptions at Volcán Mocho-Choshuenco, southern Chile. *J Volcanol Geotherm Res* 299:103–129. <https://doi.org/10.1016/j.jvolgeores.2015.04.003>
- Rawson H, Keller TM, Fontijn K, Pyle DM, Mather TA, Smith VC, Naranjo JA (2016) Compositional variability in mafic arc magmas over short spatial and temporal scales: evidence for the signature of mantle reactive melt channels. *Earth Planet Sci Lett* 456:66–77. <https://doi.org/10.1016/j.epsl.2016.09.056>
- Robidoux P, Aiuppa A, Rotolo SG, Rizzo AL, Hauri EH, Frezzotti ML (2016) Volatile contents of mafic-to-intermediate magmas at San Cristobal Volcano in Nicaragua. *Lithos* 272–273:147–163. <https://doi.org/10.1016/j.lithos.2016.12.002>
- Robidoux P, Frezzotti ML, Hauri EH, Aiuppa A (2018) Shrinkage Bubbles: The C-O-H-S Magmatic Fluid System at San Cristóbal Volcano. *J Petrol* 59(11):2093–2122. <https://doi.org/10.1093/ptrology/egy092>
- Roeder PL, Emslie RF (1970) Olivine-liquid equilibrium. *Contrib Mineral Petrol* 29(4):275–289. <https://doi.org/10.1007/BF00371276>
- Rose-Koga EF, Koga KT, Devidal J-L, Shimizu N, Le Voyer M, Dalou C, Döbeli M (2020) In-situ measurements of magmatic volatile elements, F, S, and Cl, by electron microprobe, secondary ion mass spectrometry, and heavy ion elastic recoil detection analysis. *Am Min* 105(5):616–626. <https://doi.org/10.2138/am-2020-7221>
- Ruprecht P, Bachmann O (2010) Pre-eruptive reheating during magma mixing at Quizapu volcano and the implications for the explosiveness of silicic arc volcanoes. *Geology* 38(10):919–922. <https://doi.org/10.1130/G31110.1>
- Sable JE, Houghton BF, Del Carlo P, Coltelli M (2006) Changing conditions of magma ascent and fragmentation during the 122 BC basaltic Plinian eruption: evidence from cast micro textures. *J Volcanol Geotherm Res* 158:333–354. <https://doi.org/10.1016/j.jvolgeores.2006.07.006>
- Scandone R, Cashman KV, Malone SD (2007) Magma supply, magma ascent and the style of volcanic eruptions. *Earth Planet Sci Lett* 253:513–529. <https://doi.org/10.1016/j.epsl.2006.11.016>
- Schiano P (2003) Primitive mantle magmas recorded as silicate melt inclusions in igneous minerals. *Earth-Sci Rev* 63(1–2):122–144. [https://doi.org/10.1016/S0012-8252\(03\)00034-5](https://doi.org/10.1016/S0012-8252(03)00034-5)
- Schiavi F, Provost A, Schiano P, Cluzel N (2016) P-V-T-X evolution of olivine-hosted melt inclusions during high-temperature homogenization treatment. *Geochim Cosmochim Acta* 172:1–21. <https://doi.org/10.1016/j.gca.2015.09.025>
- Schiavi F, Bolfan-Casanova N, Buso R, Laumonier M, Laporte D, Medjoubi K, Venugopal S, Gómez-Ulla A, Cluzel N, Hardiagon M (2020) Quantification of magmatic volatiles by Raman microtopography of glass inclusion-hosted bubbles. *Geochem Perspect Lett* 16:17–24. <https://doi.org/10.7185/geochemlet.2038>
- Sparks SRJ, Sigurdsson H, Wilson L (1977) Magma mixing: a mechanism for triggering acid explosive eruptions. *Nature* 267:315–318. <https://doi.org/10.1038/267315a0>
- Spilliaert N, Allard P, Métrich N, Sobolev AV (2006) Melt inclusion record of the conditions of ascent, degassing, and extrusion of volatile-rich alkali basalt during the powerful 2002 flank eruption of Mount Etna (Italy). *J Geophys Res* 111:B04203. <https://doi.org/10.1029/2005JB003934>
- Stern CR, Moreno H, López-Escobar L, Clavero JE, Lara LE, Naranjo JA, Parada MA, Skewes MA (2007) Chilean Volcanoes. In: Moreno T, Gibbons W (eds.) *The geology of Chile*, Geological Society, London, pp 147–178. <https://doi.org/10.1144/GOCH.5>
- Swanson DA, Rose TR, Fiske RS, McGeehin JP (2012) Keanakāko'i Tephra produced by 300 years of explosive eruptions following

- collapse of Kīlauea's caldera in about 1500 CE. *J Volcanol Geotherm Res* 215–216:8–25. <https://doi.org/10.1016/j.jvolgeores.2011.11.009>
- Szramek LA (2016) Mafic plinian eruptions: is fast ascent required? *J Geophys Res-Solid Earth* 121(10):7119–7136. <https://doi.org/10.1002/2016JB013208>
- Toplis MJ (2005) The thermodynamics of iron and magnesium partitioning between olivine and liquid: criteria for assessing and predicting equilibrium in natural and experimental systems. *Contrib Mineral Petrol* 149:22–39. <https://doi.org/10.1007/s00410-004-0629-4>
- Toramaru A (2006) BND (bubble number density) decompression rate meter for explosive volcanic eruptions. *J Volcanol Geotherm Res* 154(3–4):303–316. <https://doi.org/10.1016/j.jvolgeores.2006.03.027>
- Tucker JM, Hauri EH, Pietruszka AJ, Garcia MO, Marske JP, Truedell FA (2019) A high carbon content of the Hawaiian mantle from olivine-hosted melt inclusions. *Geochim Cosmochim Acta* 254:156–172. <https://doi.org/10.1016/j.gca.2019.04.001>
- Venugopal S, Moune S, Williams-Jones G (2016) Investigating the sub-surface connection beneath Cerro Negro Volcano and the El Hoyo complex, Nicaragua. *J Volcanol Geotherm Res* 325:211–224. <https://doi.org/10.1016/j.jvolgeores.2016.06.001>
- Venugopal S, Schiavi F, Moune S, Bolfan-Casanova N, Druitt T, Williams-Jones G (2020) Melt inclusion vapour bubbles: the hidden reservoir for major and volatile elements. *Sci Rep* 10:9034. <https://doi.org/10.1038/s41598-020-65226-3>
- Vetere F, Behrens H, Holtz F, Neuville DR (2006) Viscosity of andesitic melts—new experimental data and a revised calculation model. *Chem Geol* 228:233–245. <https://doi.org/10.1016/j.chemgeo.2005.10.009>
- Wallace PJ (2005) Volatiles in subduction zone magmas: concentration and fluxes based on melt inclusion and volcanic gas data. *J Volcanol Geotherm Res* 140(1–3):217–240. <https://doi.org/10.1016/j.jvolgeores.2004.07.023>
- Wallace PJ, Carmichael ISE (1992) Sulfur in basaltic magmas. *Geochim Cosmochim Acta* 56(5):1863–1874. [https://doi.org/10.1016/0016-7037\(92\)90316-B](https://doi.org/10.1016/0016-7037(92)90316-B)
- Wallace PJ, Carmichael ISE (1994) S speciation in submarine basaltic glasses as determined by measurements of S K- $\alpha$  X-ray wavelength shifts. *Am Mineral* 79(1–2):161–167
- Wallace PJ, Kamenetsky VS, Cervantes P (2015) Melt inclusion CO<sub>2</sub> contents, pressures of olivine crystallization, and the problem of shrinkage bubbles. *Am Mineral* 100(4):787–794. <https://doi.org/10.2138/am-2015-5029>
- Williamson BJ, Di Muro A, Horwell CJ, Spieler O, Llewellyn EW (2010) Injection of vesicular magma into an andesitic dome at the effusive–explosive transition. *Earth Planet Sci Lett* 295(1–2):83–90. <https://doi.org/10.1016/j.epsl.2010.03.027>
- Witham F, Blundy J, Kohn SC, Lesne P, Dixon J, Churakov SV, Botcharnikov RE (2012) SolEx: a model for mixed COHSCI-volatile solubilities and exsolved gas compositions in basalt. *Comput and Geosci* 45:87–97. <https://doi.org/10.1016/j.cageo.2011.09.021>
- Witter J, Kress V, Delmelle P, Stix J (2004) Volatile degassing, petrology, and magma dynamics of the Villarrica lava lake Southern Chile. *J Volcanol Geotherm Res* 134(4):303–337. <https://doi.org/10.1016/j.jvolgeores.2004.03.002>
- Zanetti A, Tiepolo M, Oberti R, Vannucci R (2004) Trace-element partitioning in olivine: modelling of a complete data set from a synthetic hydrous basanite melt. *Lithos* 75:39–54. <https://doi.org/10.1016/j.lithos.2003.12.022>
- Zimanowski B, Büttner R, Dellino P, White JDL, Wohletz KH (2015) Magma–Water Interaction and Phreatomagmatic Fragmentation. In: Sigurdsson H, Houghton B, McNutt SR, Rymer H, Stix J (eds) *The Encyclopedia of Volcanoes Second Edition*, Academic Press, San Diego, pp 473–484. <https://doi.org/10.1016/B978-0-12-385938-9.00026-2>
- Zhang Y (1999) A criterion for the fragmentation of bubbly magma based on brittle failure theory. *Nature* 402:648–650. <https://doi.org/10.1038/45210>